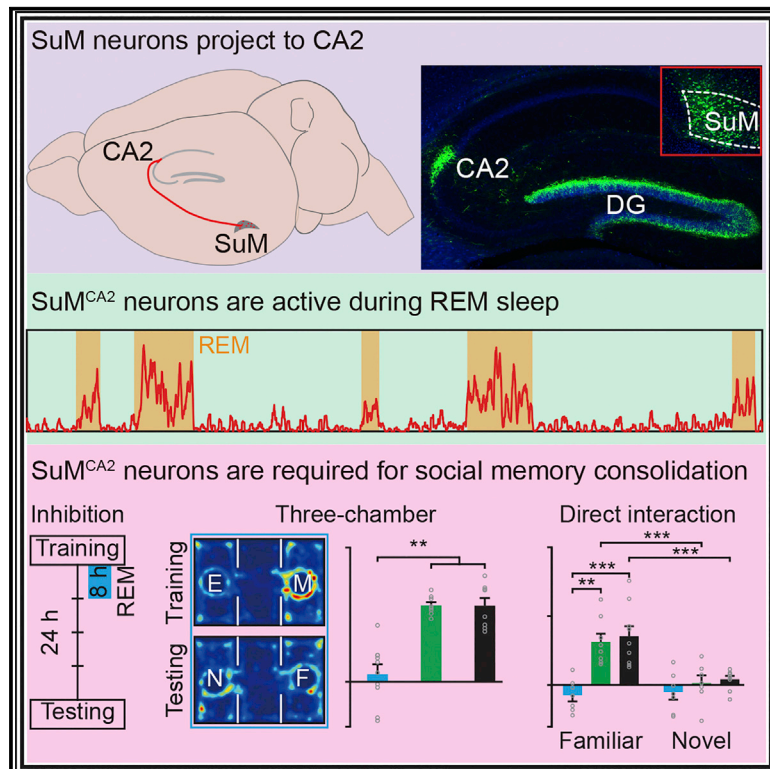


REM sleep-active hypothalamic neurons may contribute to hippocampal social-memory consolidation

Graphical abstract



Authors

Han Qin, Ling Fu, Tingliang Jian, ..., Hongbo Jia, Arthur Konnerth, Xiaowei Chen

Correspondence

xiaowei_chen@tmmu.edu.cn (X.C.), qinhan@cqu.edu.cn (H.Q.)

In brief

Qin et al. identify two groups of REM sleep-active supramammillary neurons, one projecting to the hippocampal CA2 and the other to the dentate gyrus. They find that these two cell groups critically contribute to REM-sleep-associated consolidation of social and spatial memories, respectively.

Highlights

- Both SuM-CA2- and SuM-DG-projecting neurons are highly active during REM sleep
- REM-sleep-selective silencing of SuM^{CA2} neurons impairs social memory
- REM-sleep-selective silencing of SuM^{DG} neurons impairs spatial but not social memory
- CA2^{SuM}-recipient neurons are highly active during REM sleep



Article

REM sleep-active hypothalamic neurons may contribute to hippocampal social-memory consolidation

Han Qin,^{1,2,12,*} Ling Fu,^{3,12} Tingliang Jian,^{2,4} Wenjun Jin,² Mengru Liang,^{2,5} Jin Li,² Qianwei Chen,² Xinyu Yang,¹ Haoran Du,¹ Xiang Liao,¹ Kuan Zhang,² Rui Wang,² Shanshan Liang,² Jiwei Yao,¹ Bo Hu,⁶ Shuancheng Ren,⁶ Chunqing Zhang,⁶ Yanjiang Wang,⁶ Zhian Hu,⁶ Hongbo Jia,^{7,8,9,10} Arthur Konnerth,^{7,8} and Xiaowei Chen^{2,11,13,*}

¹Center for Neurointelligence, School of Medicine, Chongqing University, Chongqing 400044, China

²Brain Research Center and State Key Laboratory of Trauma, Burns, and Combined Injury, Third Military Medical University, Chongqing 400038, China

³Britton Chance Center for Biomedical Photonics, Wuhan National Laboratory for Optoelectronics-Huazhong University of Science and Technology, Key Laboratory for Biomedical Photonics of Ministry of Education, School of Engineering Sciences, Huazhong University of Science and Technology, Wuhan 430074, China

⁴Farm Animal Genetic Resources Exploration and Innovation Key Laboratory of Sichuan Province, Sichuan Agricultural University, Chengdu 611130, China

⁵Department of Anatomy, School of Basic Medical Sciences, Anhui Medical University, Hefei 230032, China

⁶Institute of Brain and Intelligence, Third Military Medical University, Chongqing 400038, China

⁷Advanced Institute for Brain and Intelligence, Guangxi University, Nanning 530004, China

⁸Institute of Neuroscience and the Munich Cluster for Systems Neurology, Technical University of Munich, 80802 Munich, Germany

⁹Brain Research Instrument Innovation Center, Suzhou Institute of Biomedical Engineering and Technology, Chinese Academy of Sciences, Suzhou 215163, China

¹⁰Combinatorial Neuroimaging Core Facility, Leibniz Institute for Neurobiology, 39118 Magdeburg, Germany

¹¹Chongqing Institute for Brain and Intelligence, Guangyang Bay Laboratory, Chongqing 400064, China

¹²These authors contributed equally

¹³Lead contact

*Correspondence: xiaowei_chen@tmmu.edu.cn (X.C.), qinhan@cqu.edu.cn (H.Q.)

<https://doi.org/10.1016/j.neuron.2022.09.004>

SUMMARY

The hippocampal CA2 region plays a key role in social memory. The encoding of such memory involves afferent activity from the hypothalamic supramammillary nucleus (SuM) to CA2. However, the neuronal circuits required for consolidation of freshly encoded social memory remain unknown. Here, we used circuit-specific optical and single-cell electrophysiological recordings in mice to explore the role of sleep in social memory consolidation and its underlying circuit mechanism. We found that SuM neurons projecting to CA2 were highly active during rapid-eye-movement (REM) sleep but not during non-REM sleep or quiet wakefulness. REM-sleep-selective optogenetic silencing of these neurons impaired social memory. By contrast, the silencing of another group of REM sleep-active SuM neurons that projects to the dentate gyrus had no effect on social memory. Therefore, we provide causal evidence that the REM sleep-active hypothalamic neurons that project to CA2 are specifically required for the consolidation of social memory.

INTRODUCTION

Social memory is a fundamental cognitive process that enables animals to recognize and remember members of their same species, and is often impaired in neurological disorders (Lai et al., 2005; Thor and Holloway, 1982). The circuit mechanisms underlying how social memory is encoded, expressed, and consolidated are only partially understood. Accumulating evidence indicates that hippocampal CA2 neurons can respond to external social novelty signals and are necessary for encoding social memory (Alexander et al., 2016; Donegan et al., 2020; Hitti and

Siegelbaum, 2014; Wu et al., 2021). These CA2 signals are transmitted to the ventral CA1, where social memory is probably stored (Meira et al., 2018; Okuyama et al., 2016). A recent study has identified a glutamatergic neuronal circuit from the hypothalamic supramammillary nucleus (SuM) to the CA2 region that contributes to the detection of social novelty signals (Chen et al., 2020). However, while optogenetically activating the SuM^{CA2} circuit can affect social memory expression, inhibiting the same circuit does not seem to affect the same memory expression, indicating a possible contribution of other unknown circuits to the expression of social memory (Chen et al., 2020).



This possible redundancy at circuit level raises a critical question about how and through which specific circuits social memory can be consolidated in the hippocampus.

Our understanding of the function of sleep on memory consolidation has been strongly boosted by recently developed high-precision recording and manipulation approaches. Both the two stages of sleep, non-rapid-eye movement (NREM) and rapid-eye movement (REM) sleep, have been suggested to be crucial for memory consolidation (see review; Girardeau and Lopes-dos-Santos, 2021). These memory consolidation processes rely on multiple neural circuits in hippocampal and extra-hippocampal regions (Born et al., 2006; Girardeau and Lopes-dos-Santos, 2021; Marshall and Born, 2007). The prevailing concept in the field is that, during NREM sleep, the reactivation of hippocampal neurons during sharp-wave ripples (SWRs) promotes memory consolidation (Born et al., 2006; Buzsaki, 2015; Diekelmann and Born, 2010; Pfeiffer, 2020; Rasch and Born, 2013). Such reactivation during SWRs arises from CA3 and is needed for spatial memory consolidation (Ego-Stengel and Wilson, 2010; Fernandez-Ruiz et al., 2019; Girardeau et al., 2009). Similarly, Oliva et al. (2020) have suggested that the reactivation of CA2 pyramidal neurons during SWRs is essential for social-memory consolidation. In addition to the contribution of NREM sleep, REM sleep may contribute to social-memory consolidation as well (Diekelmann and Born, 2010; Maquet, 2001; Maquet et al., 1996; Stickgold, 2005). Indeed, in the case of spatial memory, a sleep-stage-specific perturbation of REM-sleep-dependent neuronal activity in the medial septum or the hippocampal dentate gyrus (DG) impairs its consolidation (Boyce et al., 2016; Kumar et al., 2020).

In the present study, we combined optical Ca^{2+} recordings, single-cell electrophysiology, and optogenetics in defined hypothalamic-hippocampal circuits during various behavioral conditions to explore the possible roles of NREM and REM sleep in mice for the consolidation of social memory. We demonstrate a surprisingly small group of CA2-projecting neurons in the hypothalamic SuM that is active exclusively during REM sleep but not during NREM sleep or quiet wakefulness (QW). Optogenetic silencing experiments revealed an essential role for these neurons in consolidating social memory. By contrast, a distinctly different group of hypothalamic SuM neurons that project to DG, which is also highly active during REM sleep, selectively contributes to consolidating spatial but not social memory. Overall, our results decisively extend the understanding of the memory function of REM sleep and highlight the importance of surprisingly small clusters of hypothalamic neurons in the consolidation of content-specific hippocampal memories. Moreover, our data advance the knowledge of the functional roles of SuM, which has recently been shown to participate in wakefulness (Pedersen et al., 2017), detection of novelty signals (Chen et al., 2020), spike-timing coordination (Ito et al., 2018), and locomotion (Farrell et al., 2021).

RESULTS

SuM^{CA2} projections are strongly active during REM sleep

SuM neurons project into two different hippocampal subfields, namely the CA2 region and DG, in a segregated manner (Vertes,

1992). We selectively labeled the SuM^{CA2} projection that is crucial for social novelty detection (Chen et al., 2020) (Figure 1A) by locally injecting an adeno-associated viral (AAV) vector expressing enhanced green fluorescent protein (EGFP) into SuM (Figure 1B, insert). We observed robust EGFP expression in cell bodies of SuM neurons one month after AAV-EGFP injection (Figures 1B and S1), and EGFP expression was also observed in axonal terminals within the CA2 region (Figures 1C and S1). In addition, we observed extensive EGFP expression in axonal terminals of SuM neurons in the DG region (Figures 1C and S1). Immunohistological staining of PCP4, a marker for CA2 pyramidal cells and DG granule cells (Lein et al., 2005), showed that axonal terminals of SuM neurons were mainly distributed in the pyramidal cell layer of CA2 and the granule cell layer of DG (Figure S2). To characterize the pattern of distribution of cell bodies of CA2-projecting neurons within SuM, we injected a small volume of the retrograde tracing indicator cholera toxin subunit B conjugated with Alexa 555 (CTB555) into CA2 (Figures S3A–S3F). Serial sectioning showed that CTB-positive neurons were bilaterally distributed in lateral SuM (Figure S3C), but the number of CTB-positive neurons in the ipsilateral SuM was approximately 3-fold of that on the contralateral side (Figures S3D and S3F; ipsilateral 89 ± 11 cells versus contralateral 30 ± 6 cells; total cell count from both sides: 119 ± 16 ; $n = 9$ mice). Moreover, these CA2-projecting neurons were largely non-overlapping with DG-projecting neurons in SuM (CTB488-labeled neurons; Figures S3B–S3F; total cell count from both sides for DG projecting neurons: 354 ± 23 ; overlapping neurons: 8 ± 2 ; $n = 9$ mice).

Although SuM neurons are highly active during both REM sleep and waking periods, as indicated by previous FOS (a marker of active neurons) immunostaining studies (Renouard et al., 2015), the activities of SuM neurons that specifically project to CA2 (SuM^{CA2}-projecting neurons) have not yet been recorded across sleep-wakefulness cycles. To do so, we first used a circuit-specific fiber photometry approach (Gunaydin et al., 2014; Qin et al., 2018) simultaneously with electroencephalogram (EEG) and electromyogram (EMG) recordings in freely moving mice. We expressed the genetically-encoded Ca^{2+} sensor jRCaMP7b in axons of SuM neurons by locally injecting AAV-syn-axon-jRCaMP7b (Broussard et al., 2018; Dana et al., 2019) into SuM and verified its expression area in SuM by post-hoc histology (Figures S3G and S3H). One month following the AAV injection, the tip of an optical fiber was implanted just above CA2 to record activity at the afferent axonal projection from the local population of SuM neurons. We routinely attached EEG and EMG electrodes to the mouse cortical surface and neck muscles, respectively, to define sleep-wakefulness states (Figure 1D, left). The axonal expression of jRCaMP7b and the optical fiber location in CA2 were verified by post-hoc histology (Figure 1D, right). Significantly, axonal terminals of SuM^{CA2}-projecting neurons exhibited a much higher level of Ca^{2+} activity during REM sleep than during either QW (indicated by their recorded behavior and EEG-EMG data) (Liu et al., 2020) or NREM sleep (Figures 1E and 1F; also see statistics in Table S1 for all figures). In addition, this activity increased strongly during NREM-REM transitions, and decreased strongly during REM-QW transitions (Figures 1G–1J).

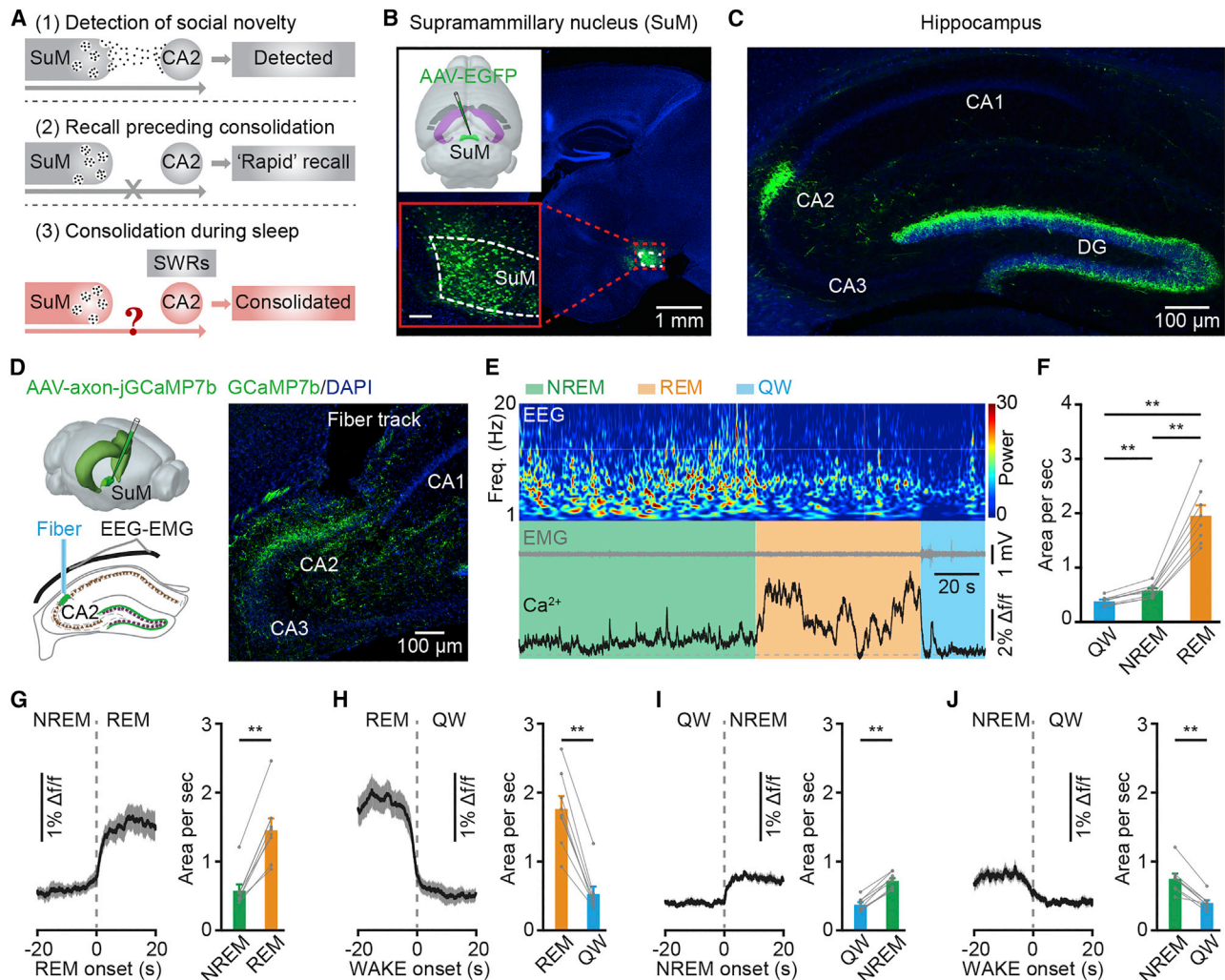


Figure 1. Strong activation of SuM^{CA2} projection terminals during REM sleep

(A) Working hypothesis for the SuM^{CA2} projection in (1) detection, (2) recall preceding consolidation, and (3) consolidation of social memory. The SuM^{CA2} projection is crucial for social novelty detection but not for social memory recall (note that we here called “rapid” recall, as it was tested 1 h after the learning trial and preceding sleep-dependent consolidation according to the previous study [Chen et al., 2020]). In addition, the reactivation of CA2 neurons during SWRs is essential for social memory consolidation. Here, we asked whether and how the SuM^{CA2} projection would contribute to social memory consolidation during sleep.

(B) Diagram of virus injection (insert) and representative histological image showing EGFP-labeled cell bodies in SuM. Scale bar, 100 μm.

(C) EGFP-labeled SuM neuron axonal terminals in the DG and CA2.

(D) Schematic of jGCaMP7b labeling, axon-fiber photometry, and EEG/EMG recordings (left); representative post-hoc histological image of a recording site in CA2 (right).

(E) Ca²⁺ activities in axonal terminals of the SuM^{CA2} projection across sleep-wakefulness cycles. Color map indicates power spectrum (μV²) of EEG. Freq., frequency; QW, quiet wakefulness.

(F) Summary of the area under the curve per second during QW, NREM, and REM sleep. Friedman’s ANOVA and Wilcoxon signed-rank tests, n = 8 mice.

(G–J) Ca²⁺ activities during state transitions: NREM to REM (G), REM to QW (H), QW to NREM (I), NREM to QW (J). Wilcoxon signed-rank test, n = 8 mice. See Table S1 for full results of statistical tests; **p < 0.01.

SuM^{CA2}-projecting neurons are highly active during REM sleep

To characterize the spike firing pattern of SuM^{CA2}-projecting neurons at the single-cell level during REM sleep, we conducted optrode recordings across sleep-wakefulness cycles (Liu et al., 2020; Stark et al., 2012). To specifically label SuM^{CA2}-projecting neurons with channelrhodopsin-2 (ChR2),

a Cre-dependent retrograde AAV (retroAAV-Cre) was injected into CA2 and, concurrently, an AAV vector carrying DIO-ChR2-mCherry was injected into the SuM. An optrode was implanted into the SuM to deliver excitatory blue light pulses and record single-unit activities (Figure 2A; see tetrode locations in Figure S4A). SuM neurons were identified as CA2 projecting neurons based on their reliable, light-induced spike responses

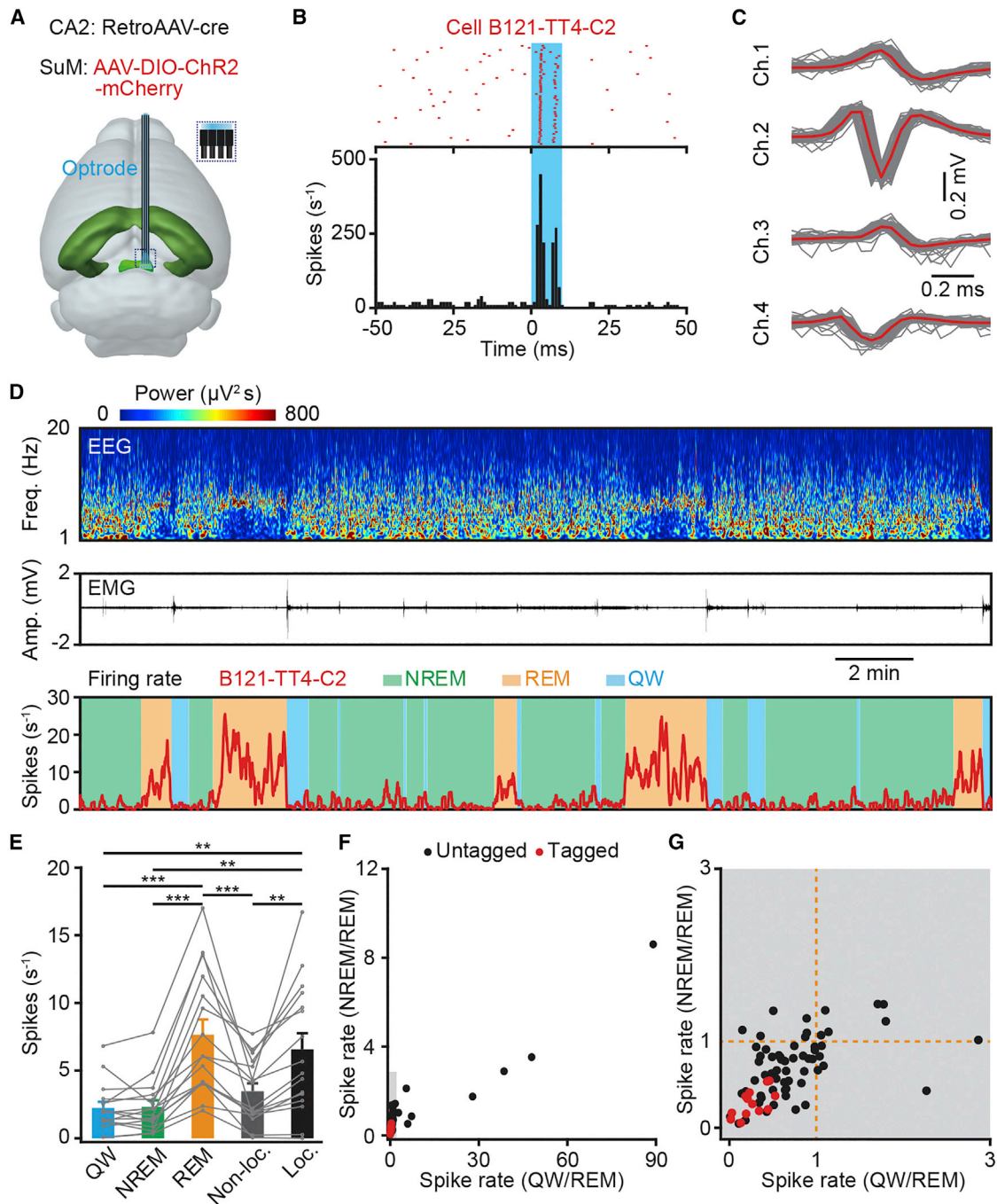


Figure 2. Single SuM^{CA2}-projecting neurons are highly active during REM sleep

(A) Experimental design for virus injection and optrode implantation in the SuM^{CA2} projection.

(B) Histogram of stimulus time for spikes in a representative SuM^{CA2}-projecting neuron (Cell#B121-TT4-C2).

(C) Waveforms of spontaneous (gray) and light-induced (red) spikes from the unit in (B).

(D) Firing rate of the neuron in (B) across sleep-wakefulness cycles. Freq., frequency; QW, quiet wakefulness.

(E) Firing rates of 16 tagged SuM^{CA2}-projecting neurons in different behavioral states. Friedman's ANOVA and Wilcoxon signed-rank tests, $n = 8$ mice. Non-loc., active waking without locomotion; Loc., locomotion.

(F and G) Distribution of firing rates during NREM and QW of tagged and untagged SuM neurons; firing rates were normalized to REM ($n = 16$ tagged cells, and 72 untagged cells).

See [Table S1](#) for full results of statistical tests; ** $p < 0.01$, *** $p < 0.001$.

(latency 3.0 ± 0.3 ms, correlation coefficient 0.93 ± 0.02 , success rate $>90\%$, $n = 16$ cells; [Figures 2B and 2C](#), and [S4C–S4E](#)). We found that, without exception, all SuM^{CA2}-projecting neurons ($n = 16/16$ units from 10 mice) significantly increased their firing rates following the transition from NREM sleep to REM sleep and again significantly decreased their firing rates following the switch from REM sleep to QW (see an example in [Figure 2D](#) and statistics in [Figure 2E](#); REM, 7.7 ± 1.1 Hz, NREM, 2.3 ± 0.5 Hz, QW, 2.2 ± 0.4 Hz; Friedman's ANOVA and Wilcoxon signed-rank tests, $n = 16$ units from 10 mice). Since a previous study has reported that the activity of SuM neurons is strongly coupled with locomotion ([Farrell et al., 2021](#)), we analyzed the activity of the SuM^{CA2}-projecting neurons during locomotion and during active waking without locomotion. We found that the firing rates of these neurons during locomotion were significantly higher than those recorded during active waking without locomotion or during NREM sleep or QW ([Figure 2E](#); locomotion, 6.6 ± 1.2 Hz, non-locomotion, 3.5 ± 0.6 Hz; Wilcoxon signed-rank test, locomotion versus non-locomotion, $p < 0.01$; locomotion versus NREM, $p < 0.01$; locomotion versus QW, $p < 0.01$; $n = 16$ tagged neurons) but not significantly different from those recorded during REM sleep ($p = 0.13$). These results suggest that SuM^{CA2}-projecting neurons are highly active during REM sleep, reaching levels that are comparable to the activity levels observed during locomotion ([Farrell et al., 2021](#)).

We analyzed the firing patterns of untagged neurons recorded with the same tetrodes and found that half of these neurons were highly active during REM sleep while the other half were highly active during NREM sleep or QW (with 54% REM active, 17% NREM active, and 29% wake active, $n = 72$ untagged units; [Figures 2F and 2G](#)). In addition to the hippocampal projection, many of these untagged neurons may also project to other regions such as the prefrontal cortex, medial septum, and lateral hypothalamus, regions that are involved in arousal, locomotion, or other brain functions ([Farrell et al., 2021](#); [Pan and McNaughton, 2004](#); [Pedersen et al., 2017](#)).

The above results suggest that SuM^{CA2}-projecting neurons receive inputs from REM sleep-active brain regions. To test this possibility, we performed a retrograde transsynaptic tracing experiment ([Figure S5](#)). We found that, in addition to the regions reported in the previous study ([Chen et al., 2020](#)), the upstream regions of SuM^{CA2} neurons indeed included those sites that are related to the generation or regulation of REM sleep, including the subcoeruleus nucleus (SLD) ([Lu et al., 2006](#)), the laterodorsal tegmental nucleus (LDT), the pedunculopontine tegmental nucleus (PPTg) ([Van Dort et al., 2015](#)), and the zona incerta (ZI) ([Liu et al., 2017](#)).

As social exploration has been shown to increase the number of SWRs during NREM sleep ([Oliva et al., 2020](#)), we analyzed the firing rates of the REM-active neurons in the SuM after social exploration ([STAR Methods](#)). We found that the firing rates of these neurons increased significantly during REM sleep but not during NREM sleep or QW ([Figure S6](#), Wilcoxon signed-rank test, QW: $p = 0.24$, NREM: $p = 0.74$, REM: $p < 0.001$). These results suggest that REM-active neurons in the SuM may contribute to social learning and memory.

SuM^{DG}-projecting neurons are highly active during REM sleep

A group of SuM neurons sends its axonal projections to the DG region ([Figures 1C and S1](#)), but the activity patterns during sleep-wakefulness cycles of this SuM^{DG} axonal projection remain uncharacterized. We used the same approach as described above and monitored SuM^{DG} projection activities at both the population and single-cell levels. The Ca²⁺ indicator jRCaMP7b was expressed in axons of SuM neurons by AAV-axon-jRCaMP7b injection into the SuM. After virus expression, optical fiber was implanted above the DG ([Figure 3A](#)). The virus expression and fiber location were verified by post-hoc histology ([Figure 3B](#)). Fiber photometry recordings of SuM^{DG} axonal terminal populations showed a much higher level of activity during REM sleep than that during NREM sleep or QW ([Figures 3C and 3D](#)). The changes in activity in the SuM^{DG} projection during sleep-wakefulness transitions were strikingly similar to those recorded in the SuM^{CA2} projection ([Figures 3E–3H](#)).

Optrode recordings were applied to SuM^{DG}-projecting neurons by the same procedure as described above ([Figure 4A](#)). The tetrode locations were confirmed by post-hoc histology ([Figure S4B](#)). SuM neurons were identified as DG projecting neurons based on their reliable, light-induced spike responses (latency 2.6 ± 0.4 ms, correlation coefficient 0.92 ± 0.02 , success rate $>90\%$, $n = 19$ cells; [Figures 4B and 4C](#), and [S4C–S4E](#)). The results showed that virtually all SuM^{DG}-projecting neurons exhibited significantly higher firing rates during both REM sleep and locomotion than during NREM sleep, QW, or active waking without locomotion ([Figures 4D and 4E](#); REM, 11.9 ± 2.3 Hz, locomotion, 13.8 ± 4.3 Hz, NREM, 2.6 ± 0.8 Hz, QW, 3.3 ± 1.0 Hz, non-locomotion 5.2 ± 2.3 Hz; Friedman's ANOVA and Wilcoxon signed-rank tests, $n = 19$ tagged neurons from 7 mice). Thus, these results indicate that the parallel SuM-to-CA2 and SuM-to-DG projections are both highly active during REM sleep or locomotion but not during NREM sleep, QW, or active waking without locomotion.

REM-sleep-selective silencing of SuM^{CA2}-projecting neurons impairs social but not spatial memory

The strong activation of the SuM^{CA2} projection exclusively during REM sleep suggests that this projection plays a possible role in social memory consolidation. To test this hypothesis, we tested social memory in mice after selectively silencing this projection during REM sleep by axonal projection-specific optogenetic inhibition. To do so, the inhibitory protein *Guillardia theta* anion-conducting channelrhodopsin 1 (GtACR1) ([Govorunova et al., 2015](#)) was specifically expressed in SuM^{CA2} projecting neurons by bilateral injection of retroAAV-Cre into CA2 concurrent with AAV-DIO-GtACR1-mCherry injection into SuM ([Figure 5A](#); see the silencing effect on spike firing by GtACR1 activation in [Figures S7A and S7B](#); see fiber tip locations in [Figure S7C](#)). We first examined whether silencing of SuM^{CA2}-projecting neurons had an effect on hippocampal CA1 activity during REM sleep by analyzing local field potentials (LFP) and neuronal firing rates. We observed that photoinhibition had no effect on either dorsal CA1 LFP activity in the frequency range of 0–30 Hz (including delta, theta, alpha, and beta rhythms; [Figures 5A–5D](#)) or neuronal firing (pre: 12.1 ± 3.4 , inhibition: 12.8 ± 3.7 ,

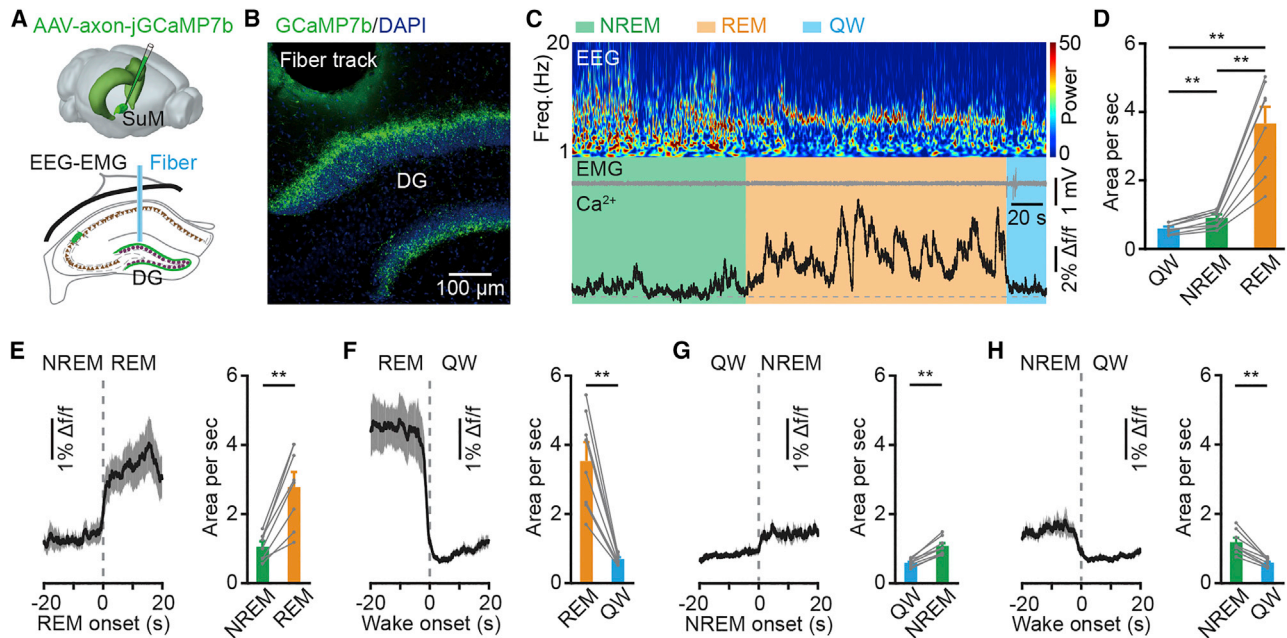


Figure 3. Strong activation of SuM^{DG} projection terminals during REM sleep

(A and B) Axonal terminal recording in the DG by fiber photometry after AAV-axon-jGCaMP7b injection into SuM. (A) Schematic of virus injection and optical fiber, EEG, EMG recordings. (B) Post-hoc histological confirmation of jGCaMP7b expression and fiber position in the DG. (C) Ca²⁺ activities in axonal terminals of the SuM^{DG} projection across sleep-wakefulness cycles. Color map indicates power spectrum (μV^2) of EEG. (D) Summary of the area under the curve per second during QW, NREM, and REM sleep. Friedman's ANOVA and Wilcoxon signed-rank tests, $n = 8$ mice. (E–H) Ca²⁺ activities during state transitions. Wilcoxon signed-rank test, $n = 8$ mice. See Table S1 for full results of statistical tests; ** $p < 0.01$.

post: 12.6 ± 3.7 ; RMs 1-way ANOVA test, $p = 0.48$, $n = 16$ cells from 7 mice). In addition, we found that inhibition of SuM^{CA2}-projecting neurons during REM sleep did not alter CA2 LFP power (Figures S8A–S8E). These results differed from previously reported work in which silencing of a different projection, emerging from medial septum GABAergic neurons, significantly reduced the theta rhythm in the dorsal CA1 (Boyce et al., 2016).

We then conducted a three-chamber test (Hitti and Siegelbaum, 2014; Moy et al., 2004), an established social memory behavior task, to investigate the influence of silencing SuM^{CA2}-projecting neurons during REM sleep on social memory consolidation. During the training phase, a subject mouse was allowed to freely explore in a chamber with an unfamiliar mouse versus an empty chamber for 20 min (Figure 5E). A social preference index was calculated based on the cumulative exploration times in the two chambers (STAR Methods). The subject mice showed a significant preference for the chamber with a stimulus mouse in the day 1 training phase (Figure 5F top; 175.7 ± 14.6 s versus 55.1 ± 5.3 s; $p = 0.000008$, Wilcoxon signed-rank test, $n = 26$ mice). There was no significant difference in the social preference index among the GtACR1 REM, mCherry REM, GtACR1 NREM/QW, and GtACR1 NREM groups (Figures 5G and S9; $p = 0.79$, 1-way ANOVA test). During the first 8 h of the memory consolidating stages following training, blue light for optogenetic stimulation was delivered through the implanted optical fiber to SuM^{CA2}-projecting neurons in the GtACR1 REM group or mCherry REM group ~ 6 s after

REM sleep was detected. Exposure to blue light persisted until the end of each REM sleep episode. A second control group of mice expressing GtACR1 in SuM^{CA2}-projecting neurons (GtACR1 NREM/QW) underwent the same procedure as the GtACR1 REM group, except that the blue light was delivered during either NREM sleep or QW episodes with the similar amount of time to what was delivered for the GtACR1 REM group (STAR Methods; see the distribution of the onset of light stimulation relative to the beginning of the 8-h recording in Figure S10). In a third control group (GtACR1 NREM), we delivered blue light for inhibition during a large fraction (>70%) of NREM sleep episodes (STAR Methods). In total, blue light was delivered for approximately $87.5 \pm 0.7\%$ of the cumulative REM sleep time ($2,151 \pm 138$ s, $n = 10$ GtACR1 REM mice and $2,086 \pm 154$ s, 8 mCherry REM mice; Figure S10). This REM-sleep-selective silencing of SuM^{CA2}-projecting neurons did not affect the structure of sleep patterns as indicated by the following four parameters: REM sleep episode duration, total REM sleep time, NREM sleep episode duration, and total NREM sleep time (Figures S10C and S10D).

On day 2 of testing, the subject mouse was allowed to freely investigate a chamber with a familiar mouse, followed by the visit of another chamber with a novel mouse. Mice often preferentially interact intensively with novel conspecifics (Hitti and Siegelbaum, 2014; Moy et al., 2004). We therefore compared such preference for novel mice between the GtACR1 and control groups. We found that mice of the GtACR1 REM group showed no preference for

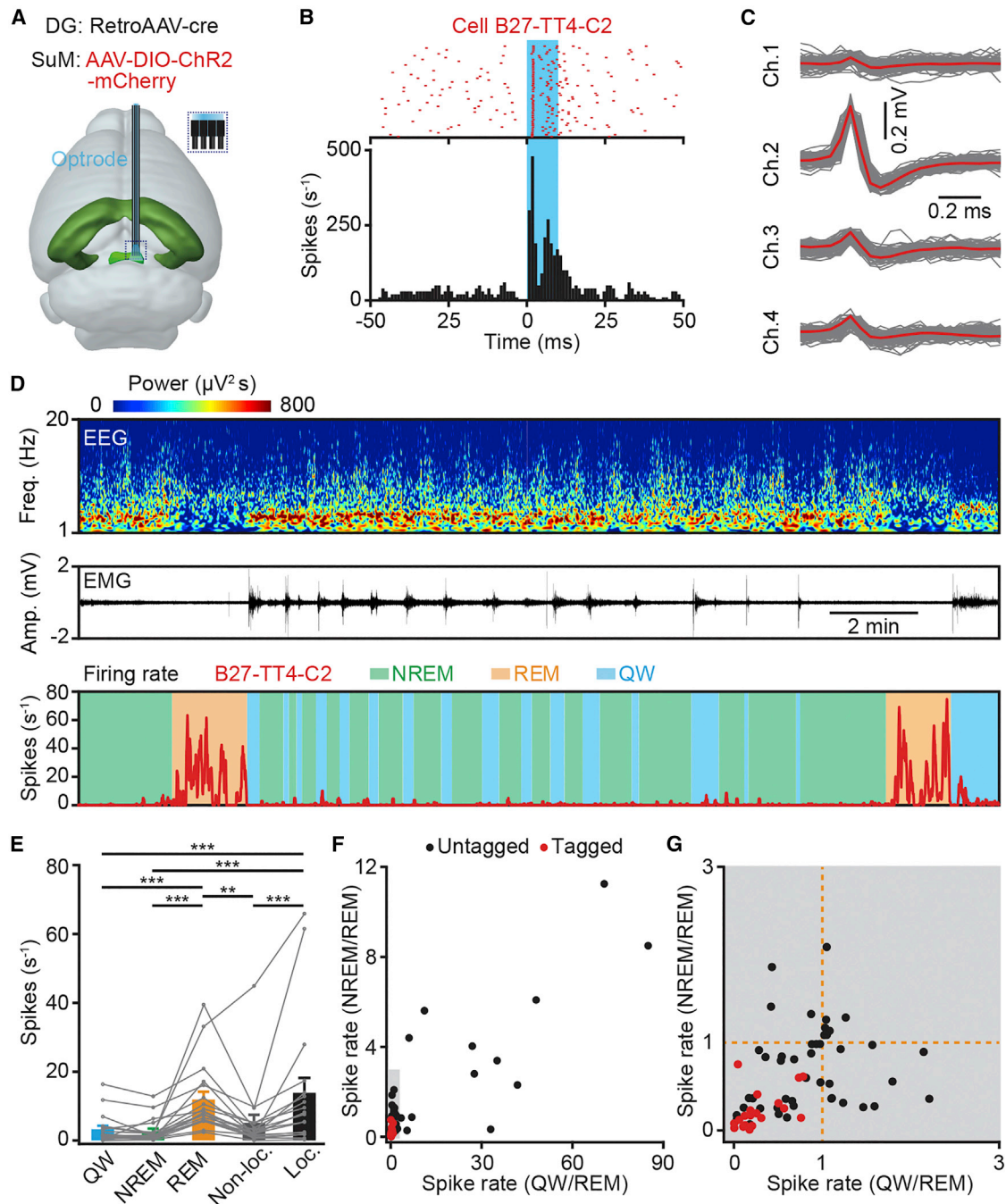


Figure 4. Single SuM^{DG}-projecting neurons are highly active during REM sleep

(A) Diagram showing virus injection and optrode implantation in the SuM^{DG} projection.

(B) Stimulus time histogram of spikes in a representative SuM^{CA2}-projecting neuron (Cell#B27-TT4-C2).

(C) The waveforms of spontaneous (gray) and light-induced (red) spikes of the neuron in (B).

(D) Firing rates of the representative neuron across sleep-wakefulness cycles.

(E) Firing rates of 19 tagged SuM^{DG}-projecting neurons in different behavioral states. Friedman's ANOVA test and Wilcoxon signed-rank tests, $n = 8$ mice. Non-loc., active wake without locomotion; Loc., locomotion.

(F and G) Distribution of firing rates during NREM and QW of 19 tagged and 58 untagged SuM neurons, firing rate normalized to REM.

See Table S1 for full results of statistical tests; ** $p < 0.01$, *** $p < 0.001$.

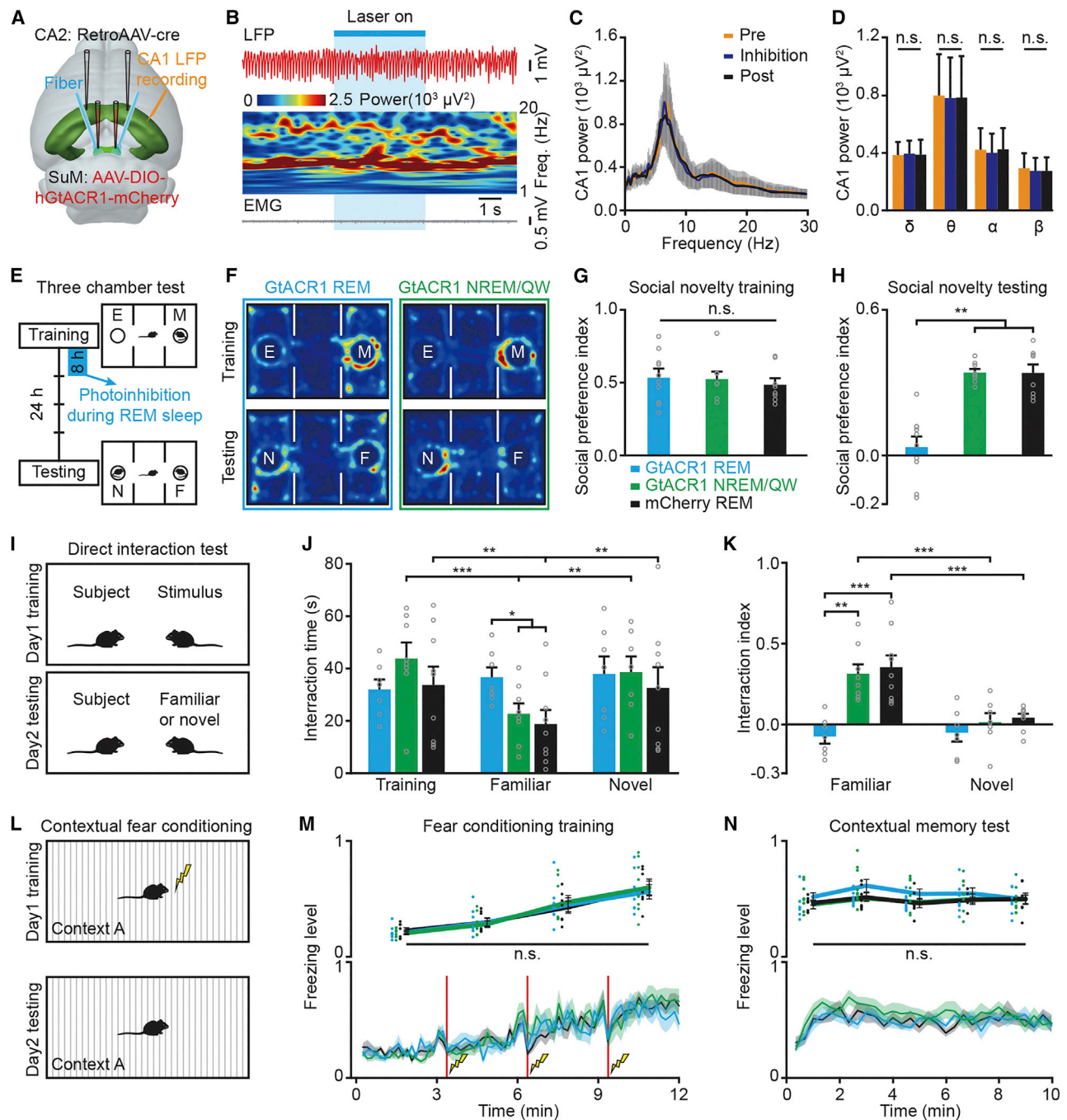


Figure 5. Optogenetic silencing of SuM^{CA2}-projecting neurons during REM sleep impairs social but not spatial memory

(A–D) Effects of silencing SuM^{CA2}-projecting neurons on CA1 local field potential (LFP) activity during REM sleep. (A) Experimental design for retrograde labeling of SuM^{CA2} neurons by GtACR1-mCherry, fiber implantation above SuM, and LFP recording in CA1. (B) Representative heatmap showing the effects of silencing SuM^{CA2} neurons on CA1 LFP during REM sleep. Freq., frequency. (C and D) CA1 LFP power spectral analysis pre-, during, and post-photoinhibition. RMs 1-way ANOVA test, $n = 7$.

(E) Protocol for optogenetics and three-chamber social memory task. E, empty; M, mouse; N, novel; F, familiar.

(F) Representative heatmaps of distribution of time in three-chamber task.

(G and H) Summary of social preference indexes in training (G) and testing (H) of the social novelty task. (G), 1-way ANOVA test; (H), Kruskal-Wallis test with Tukey post-hoc comparison test; GtACR1 REM $n = 10$, GtACR1 NREM/QW $n = 8$, mCherry REM $n = 8$.

(I) Protocol for the direct interaction (DI) test.

(legend continued on next page)

novel versus familiar mice (Figure 5F bottom left; novel, 127.0 ± 11.0 s versus familiar, 120.7 ± 13.9 s; $p = 0.49$, Wilcoxon signed-rank test, $n = 10$ mice). In contrast, the preference for novel mice was retained by animals of the GtACR1 NREM/QW group (Figure 5F bottom right; novel, 149.3 ± 29.4 s versus familiar, 73.6 ± 13.4 s; $p = 0.008$, Wilcoxon signed-rank test, $n = 8$ mice) or mCherry REM group (novel, 95.8 ± 23.7 s versus familiar, 48.3 ± 12.3 s; $p = 0.008$, Wilcoxon signed-rank test, $n = 8$ mice). Consistent with this finding, the social preference index was significantly lower in the GtACR1 REM group than in each of the control groups (Figures 5H and S9C; GtACR1 REM group versus GtACR1 NREM/QW group, $p < 0.01$; GtACR1 REM group versus mCherry REM group, $p < 0.01$; GtACR1 REM group versus GtACR1 NREM group, $p < 0.05$, Kruskal-Wallis test with Tukey post-hoc comparison test). In addition, no significant differences were observed in either locomotion speed or total locomotion time among these four groups (Figure S11A, $p > 0.05$, 1-way ANOVA test).

In addition to the three-chamber test, we next performed another social memory behavioral task, namely the direct interaction test (Hitti and Siegelbaum, 2014; Kogan et al., 2000), to test the consequences of silencing SuM^{CA2}-projecting neurons during REM sleep on social memory consolidation (Figure 5I). For this purpose, optogenetic inhibition of SuM^{CA2}-projecting neurons was performed on the subject mice that were exposed to unfamiliar mice during training for 5 min on day 1. At 24 h after training, each subject mouse was re-exposed to the same mouse or to another novel mouse for 5 min. We observed that the GtACR1 REM group interacted for a longer period (Figure 5J; 36.7 ± 3.9 s, $n = 7$ mice) with the familiar mouse than did members of the GtACR1 NREM/QW group (Figure 5J; 22.7 ± 4.0 s, $p = 0.04$, $n = 8$ mice, RMs 2-way ANOVA with Sidak post-hoc comparison test) or the mCherry REM group (Figure 5J; 18.8 ± 5.4 s, $p = 0.04$, $n = 9$ mice, RMs 2-way ANOVA with Sidak post-hoc comparison test). An interaction index was calculated to identify preferential interactions by each subject mouse with either the novel or familiar mice (STAR Methods). The GtACR1 REM group (Figure 5K; -0.07 ± 0.04 , $n = 7$ mice) showed a significantly lower interaction index (i.e., suggesting a lower familiarity) with the familiar mice than that determined for members of the GtACR1 NREM/QW group (Figure 5K; 0.31 ± 0.06 , $p < 0.01$, $n = 8$ mice, RMs 2-way ANOVA with Sidak post-hoc comparison test) or for members of the mCherry REM group (Figure 5K; 0.29 ± 0.08 , $p < 0.001$, $n = 9$ mice, RMs 2-way ANOVA with Sidak post-hoc comparison test).

We also tested the effects of REM-sleep-selective silencing of SuM^{CA2}-projecting neurons on spatial memory consolidation (Boyce et al., 2016). For this purpose, we performed, first, a contextual fear memory test and, second, a novel object position recognition (NOPR) test. For the first test, subject mice were trained using a contextual fear learning paradigm on day 1 (Figures 5L, 5M, and S12A; STAR Methods). During the next

experimental step, optogenetic inhibitory light was delivered to SuM^{CA2}-projecting neurons selectively either during REM sleep episodes (GtACR1 REM and mCherry REM groups) or during NREM/QW (GtACR1 NREM/QW group) in the first 8 h post-training period. At 24 h after training, the mice were re-exposed to the conditioned context for a duration of 10 min. Consistently, no significant differences in freezing levels were observed among these three groups (Figure 5N).

For the NOPR test, which has been previously used to test for spatial memory (Antunes and Biala, 2012; Boyce et al., 2016), mice were trained to freely explore two objects, A and B, in an arena (Figure S9D). In general, mice spent the same exploration time for objects A and B in the training phase (Figure S9E). In the next step, optogenetic silencing was selectively applied during REM sleep in the 8-h consolidation stages, as described above (see Figure 5E). At 24 h after training, mice were re-introduced to the arena with object B in a different position. Consistent with the results from the contextual fear memory test, we observed no significant difference in the discrimination index (i.e., longer exploration time indicating a lower familiarity) between the GtACR1 REM and GtACR1 NREM groups (Figure S9F; see the correlation analysis of memory performance and total REM sleep time in Figures S9G and S9H). Further, cued fear memory (a hippocampal-independent process) was not affected by silencing SuM^{CA2}-projecting neurons during REM sleep (Figure S12B; STAR Methods). These experiments indicate that the SuM^{CA2} projection is required for REM sleep-associated consolidation of social memory but has no contribution to the consolidation of spatial memory.

REM-sleep-selective silencing of SuM^{DG}-projecting neurons impairs spatial but not social memory

In light of our observations that the SuM^{DG} projection was also strongly active during REM sleep (Figures 3 and 4), we next explored its possible contribution to the consolidation of social memory. For this experiment, we specifically labeled SuM^{DG}-projecting neurons with GtACR1 by retroAAV-Cre injection into the DG and AAV-DIO-GtACR1-mCherry injection into SuM. We again tested the effect of silencing SuM^{DG}-projecting neurons on CA1 LFP and CA1 neuronal firing rates during REM sleep (Figure 6A). We found that light delivery to SuM^{DG} GtACR1⁺ neurons caused a significant reduction of CA1 LFP power in the theta, as well as in the alpha and beta bands (Figures 6B–6D), and also significantly reduced CA1 neuronal firing rates (pre: 9.2 ± 2.6 , inhibition: 7.6 ± 2.2 , post: 9.12 ± 2.6 ; RMs 1-way ANOVA test, $p = 0.014$, $n = 20$ cells from 6 mice; pre versus inhibition, $p = 0.013$, inhibition versus post, $p = 0.02$). This result is different from the absence of any effect when silencing SuM^{CA2}-projecting neurons (Figures 5A–5D). This difference suggests that SuM^{DG}-projecting neurons are more strongly modulated by theta activity than are SuM^{CA2}-projecting neurons during REM sleep, as supported by our theta coupling analysis of these

(J and K) Summary of total interaction time (J) and interaction index (K) in the DI test. RMs 2-way ANOVA with Sidak post-hoc comparison test; GtACR1 REM $n = 7$, GtACR1 NREM/QW $n = 8$, mCherry REM $n = 9$ mice.

(L) Protocol for contextual fear conditioning.

(M and N) Freezing levels during training (M) and testing (N) phases. RMs 2-way ANOVA test; GtACR1 REM $n = 8$, GtACR1 NREM/QW $n = 9$, mCherry REM $n = 7$. See Table S1 for full results of statistical tests, n.s. $p > 0.05$, ** $p < 0.01$, *** $p < 0.001$.

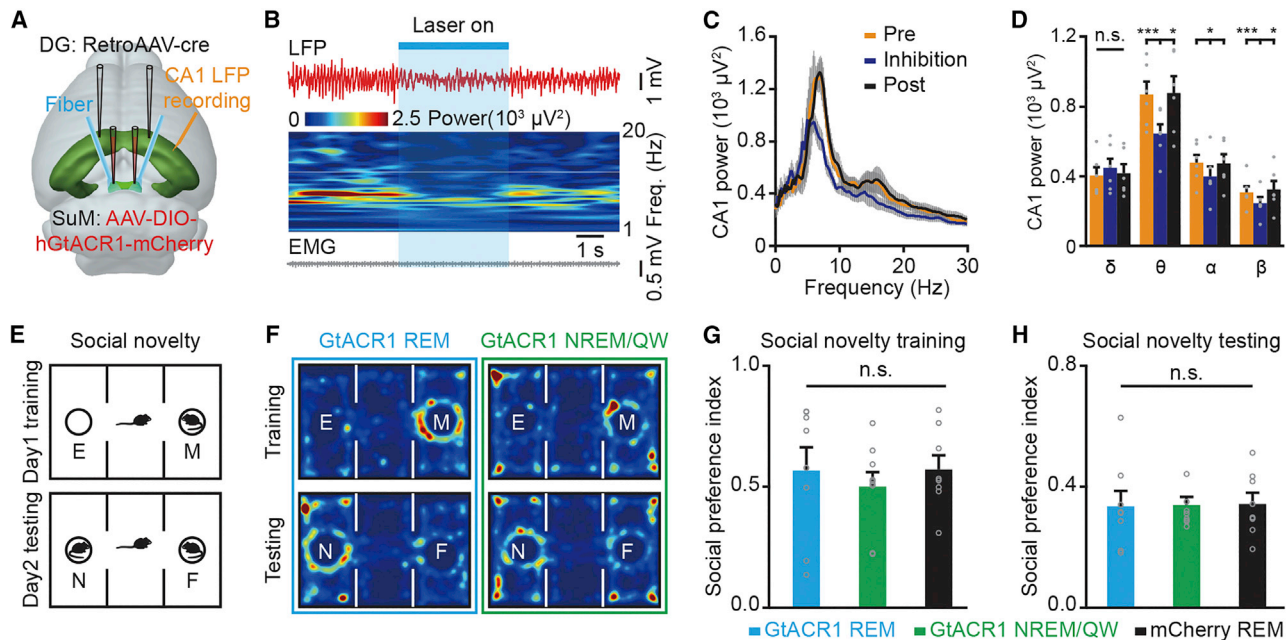


Figure 6. Optogenetic silencing of SuM^{DG}-projecting neurons during REM sleep reduces theta rhythm but does not alter social memory (A–D) Effects of silencing SuM^{DG}-projecting neurons on CA1 LFP activity during REM sleep. (A) Experimental design for labeling of SuM^{DG}-projecting neurons by GtACR1-mCherry, fiber implantation above SuM, and LFP recording in CA1. (B) Example heatmap showing the effects of silencing SuM^{DG}-projecting neurons on CA1 LFP power during REM sleep. (C and D) Spectral analysis of CA1 LFP power pre-, during, and post-photoinhibition, RMs 1-way ANOVA with LSD post-hoc comparison test, n = 6. (E) Protocol for three-chamber task. E, empty; M, mouse; N, novel; F, familiar. (F) Representative heatmaps of the distribution of mouse times in each chamber in the task. (G and H) Summary of social preference indexes in the training (G) and testing (H) phases of the three-chamber task. 1-way ANOVA test; GtACR1 REM n = 8, GtACR1 NREM/QW n = 9, mCherry REM n = 8. See Table S1 for full results of statistical tests, n.s. p > 0.05, *p < 0.05, ***p < 0.001.

two cell groups (Figure S13). In addition, we also found that inhibition of SuM^{DG}-projecting neurons during REM sleep significantly reduced DG LFP power in the theta and beta bands (Figures S8F–S8H). Next, we conducted the three-chamber social tests, as described above (Figures 6E–6H), and observed no obvious influence on the social preference index in either the GtACR1 REM group or the control groups (Figure 6H; GtACR1 REM, 0.34 ± 0.05, n = 8 mice; GtACR1 NREM/QW, 0.34 ± 0.03, n = 9 mice; mCherry REM, 0.34 ± 0.04, n = 8 mice; p = 0.99, 1-way ANOVA test).

As the SuM^{DG} projection has been found to be essential for spatial memory encoding and expression (Chen et al., 2020; Li et al., 2020), we next tested the effects of silencing SuM^{DG}-projecting neurons during REM sleep on spatial memory consolidation. We conducted contextual fear conditioning (Figure 7A), and mice were trained in a conditioned context (Figure 7B). The activity of SuM^{DG} neurons was then optogenetically inhibited, as described above. On day 2 of the memory retrieval phase, mice of the GtACR1 REM group showed a significantly lower freezing level than mice from the mCherry REM group or the GtACR1 NREM/QW group (Figure 7C). For the NOPR test, we observed a significant decrease in the discrimination index for both objects in the GtACR1 REM group, but not in the GtACR1 NREM/QW or mCherry REM group (Figure 7G; GtACR1 REM, -0.04 ± 0.01; GtACR1 NREM/QW, 0.28 ± 0.02; mCherry REM,

0.25 ± 0.03; also see Figure S14 for comparisons with SuM^{CA2} inhibition groups). Collectively, these results establish that the SuM^{DG} projection is required for REM-sleep-dependent spatial memory consolidation but does not contribute to social memory consolidation.

CA2^{SuM}-recipient neurons are highly active during REM sleep

Given that SuM projections are excitatory and release glutamate into CA2 (Chen et al., 2020; Robert et al., 2021), we expected that the increased activity of SuM neurons during REM sleep would correlate with an increase in the activity of the target CA2 neurons. To test this hypothesis, we recorded the activity of SuM recipient CA2 neurons (CA2^{SuM}-recipient neurons) by fiber photometry across sleep-wakefulness cycles. To label the CA2^{SuM}-recipient neurons specifically with a Ca²⁺ indicator, we injected the anterograde *trans*-synaptic virus construct scAAV2/1-hSyn-Cre (Zingg et al., 2017) into SuM and AAV-LOXP-GCaMP6f into CA2 (Figure 8A). Three weeks after virus injection, an optical fiber was implanted above CA2 (Figure 8B) to monitor the activity of labeled CA2 neurons. We found that these CA2 neurons showed significantly higher Ca²⁺ activity during REM sleep than during NREM sleep or QW (see an example in Figure 8C and summary in Figure 8D). Next, we used the same approach to record the activity of DG^{SuM}-recipient neurons

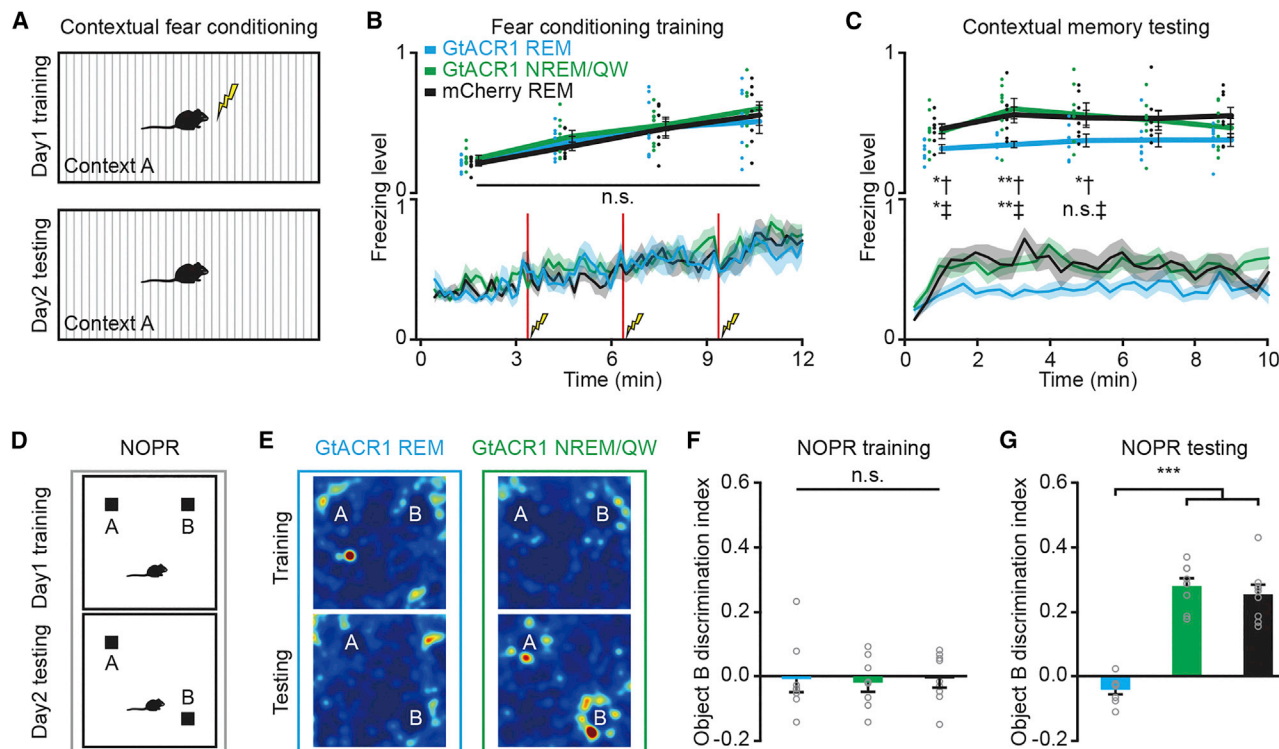


Figure 7. Optogenetic silencing of SuM^{DG}-projecting neurons during REM sleep impairs spatial memory

(A) Protocol for contextual fear conditioning.

(B and C) Freezing levels during the training (B) and testing (C) phases. RMs 2-way ANOVA with Sidak post-hoc comparison test; †GtACR1 REM (n = 8) versus mCherry REM (n = 8), ‡ GtACR1 REM (n = 8) versus GtACR1 NREM/QW (n = 8).

(D) Protocol for novel object position recognition (NOPR) task.

(E) Representative heatmaps of the distribution of mouse times spent with each object in the NOPR task.

(F and G) Summary of discrimination indexes in the training (F) and testing (G) phases of the NOPR task. 1-way ANOVA with LSD post-hoc comparison test; GtACR1 REM n = 8, GtACR1 NREM/QW n = 8, mCherry REM n = 9.

See Table S1 for full results of statistical tests, n.s. p > 0.05, *p < 0.05, **p < 0.01, ***p < 0.001.

(Figures S15A and S15B) and found that these DG neurons were highly active during REM sleep (Figures S15C and S15D). Collectively, these results suggest that the downstream CA2 and DG neurons of SuM are both highly active during REM sleep.

DISCUSSION

Sleep supports memory consolidation, but the circuit-specific mechanisms for different types of memory remain largely unknown (Blumberg et al., 2020; Diekelmann and Born, 2010; Girardeau and Lopes-dos-Santos, 2021). Currently, the prevailing general notion is that, during SWRs of NREM sleep, reactivating the participating neurons and circuits that have been active during learning leads to the consolidation of the freshly learned information (Buzsaki, 2015; Pfeiffer, 2020). Such reactivation during SWRs occurring in CA3 (Ego-Stengel and Wilson, 2010; Girardeau et al., 2009) and CA2 (Oliva et al., 2020) during NREM sleep promotes spatial and social memories respectively. However, whether and how REM sleep consolidates social memory remains elusive.

The main finding of this study is that the consolidation of social memory requires intense activity of SuM^{CA2}-projecting neurons

during REM sleep, without a detectable contribution of neuronal activity during QW or NREM sleep. An additional novel finding is that the SuM^{DG} projection selectively drives the REM-sleep-dependent consolidation of spatial but not social memory. Remarkably, the optogenetic experiments reveal that the silencing of as few as ~100 REM sleep-active SuM^{CA2}-projecting neurons is sufficient to cause major perturbations in the consolidation of social memory. Analogously, we estimate that ~350 REM sleep-active SuM neurons projecting to DG contribute the consolidation of spatial memory (Figure S3). In each case, dedicated neurons within these two small clusters are highly active exclusively during REM but not during NREM sleep or QW. Thus, these results establish the presence of two narrow but effective neuronal “gateways” from the SuM of the posterior hypothalamus to the hippocampus that control the REM-sleep-dependent consolidation of social and spatial memories with notable specificity.

The results presented here allowed us to advance and specify the working model for how the SuM^{CA2} projection participates in the processing and storage of novel social information (Figures 8E and 8F) (Chen et al., 2020; Girardeau and Lopes-dos-Santos, 2021). During a first social encounter with a non-familiar conspecific, a cluster of SuM neurons, projecting to

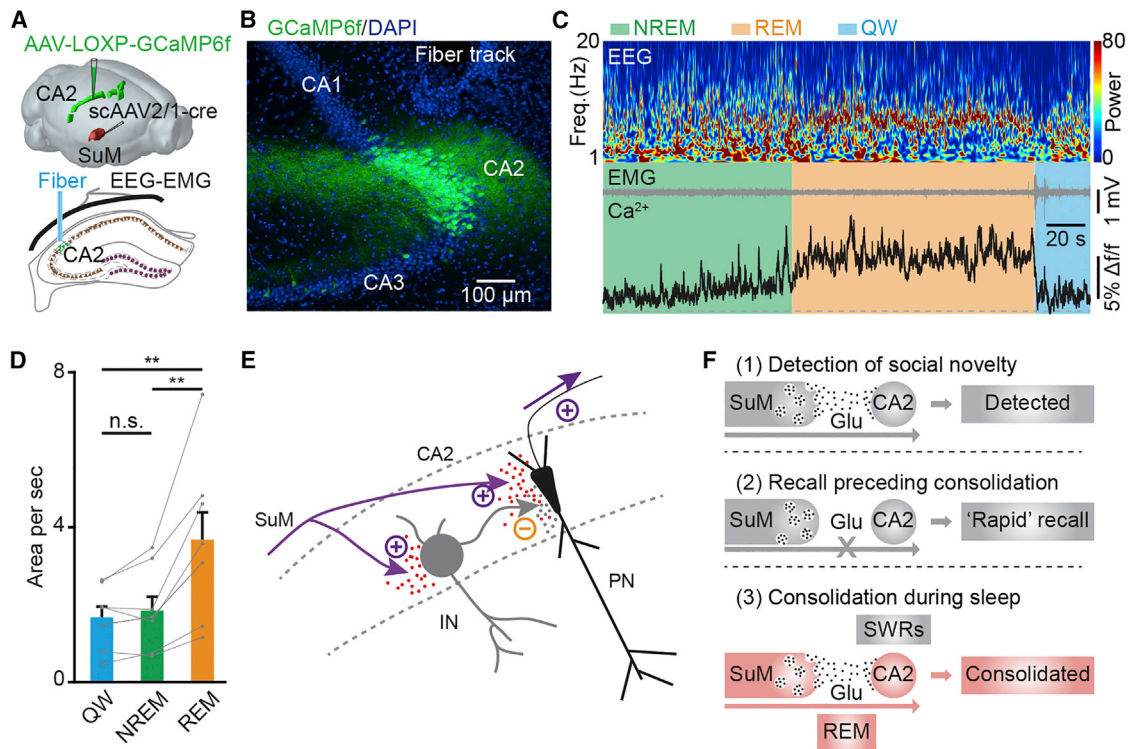


Figure 8. CA2^{SuM}-recipient neurons are highly active during REM sleep and the proposed working model

(A) Experimental design for labeling of CA2 neurons that receive inputs from SuM by the injection of scAAV2/1-Cre into SuM and AAV-LOXP-GCaMP6f into CA2, fiber implantation above CA2, and EEG-EMG recordings.

(B) Post-hoc histological confirmation of GCaMP6f expression and fiber track position in CA2.

(C) Ca²⁺ activities of CA2 neurons across sleep-wakefulness cycles. Color map indicates power spectrum (μ V²) of EEG.

(D) Summary of the area under the curve per second during QW, NREM, and REM sleep. RM 1-way ANOVA with LSD post-hoc comparison test, n = 7 mice.

(E) Model of the local circuitry of CA2 pyramidal neurons innervated by SuM projections. IN, interneuron; PN, pyramidal neurons. +, excitation; -, inhibition.

(F) Working model of the SuM^{CA2} projection for social memory consolidation during REM sleep.

See Table S1 for full results of statistical tests, n.s. p > 0.05, **p < 0.01.

the hippocampal CA2 region, is activated through afferent inputs that convey behavior-relevant sensory and other types of information. These novel social signals are then transmitted to CA2 neurons via glutamatergic afferents, thereby initiating CA2 hippocampal social novelty detection (Chen et al., 2020) (Figure 8F, the first row). The expression process of social memory may involve an additional, yet unknown, circuit mechanism, as SuM^{CA2}-projecting neurons seem to be inactive during social memory retrieval (at least for the “rapid” recall that was tested 1 h after social learning and preceding sleep-dependent consolidation according to the previous study [Chen et al., 2020]) (Figure 8F, the second row).

To test for the effectiveness of SuM activation of CA2 during REM sleep, we performed an *in vivo* experiment to directly record the activity of SuM recipient CA2 neurons (CA2^{SuM}-recipient neurons) by fiber photometry. We found a significant increase in the activity of these CA2 neurons during REM sleep (Figures 8A–8D), consistent with the increased activity of SuM^{CA2}-projecting neurons during REM sleep (Figures 1 and 2). Based on our results and the published literature, we propose a working model in which SuM neurons affect CA2 pyramidal neurons during memory consolidation through an excitatory synaptic connection to CA2

pyramidal neurons and a strong feedforward inhibitory connection via CA2 interneurons to CA2 pyramidal neurons (Chen et al., 2020; Robert et al., 2021). As a result, SuM neurons are likely to produce an activating effect on CA2 neurons during REM sleep (Figure 8E). Therefore, optogenetic inhibition of SuM may reduce the reactivation of CA2 pyramidal neurons during REM sleep and impair social memory consolidation. Altogether, during REM sleep, these CA2-projecting SuM neurons are strongly reactivated and drive the strengthening of synaptic connectivity (Ishikawa et al., 2006; Walker and Stickgold, 2006) within participating neuronal ensembles in CA2 that project to downstream ventral CA1 neurons (Hitti and Siegelbaum, 2014; Okuyama et al., 2016). This process may ultimately lead to the consolidation of social memory (Figure 8F, the third row).

Interestingly, the reactivation of CA2 neurons by SuM afferent inputs does not seem to contribute to theta rhythm generation in both CA2 and CA1, as silencing of the SuM^{CA2}-projecting neurons during REM sleep had no effect on CA2 and CA1 LFP activity. This contrasts to the SuM^{DG}-projecting neurons, whose inhibition significantly reduces theta activity in both DG and CA1. Theta coupling analysis of these two groups of neurons showed that the SuM^{DG}-projecting neurons were more strongly

modulated by theta rhythm than were the SuM^{CA2}-projecting neurons during REM sleep (Figure S13). These results, which suggest that SuM transmits theta rhythm to CA1 through the DG projection but not the CA2 projection, advance our understanding of the role of SuM in the regulation of hippocampal CA1 population activity during REM sleep (Farrell et al., 2021).

In summary, we suggest that the REM-sleep-dependent reactivation of a specific SuM^{CA2} connectivity that is active during recent social behavior, together with the SWR-related reactivation of CA2 “social” neurons during NREM sleep (Oliva et al., 2020), may represent an integral mechanism for sleep-induced social memory consolidation (Buzsáki, 1989) (Figure 8F, the third row). In the future, an experiment to demonstrate a “reactivation” of neurons that have been active during encoding of the social events is required. In addition, loss-of-function experiments (e.g., optogenetic inhibition) could prove a causal link between the activity of SuM^{CA2}-projecting neurons and the reactivation of CA2 neurons during REM sleep, as our activity recording experiments performed in SuM^{CA2}-projecting neurons and CA2^{SuM}-recipient neurons only provided correlational evidence.

STAR★METHODS

Detailed methods are provided in the online version of this paper and include the following:

- **KEY RESOURCES TABLE**
- **RESOURCE AVAILABILITY**
 - Lead contact
 - Materials availability
 - Data and code availability
- **EXPERIMENTAL MODEL AND SUBJECT DETAILS**
- **METHOD DETAILS**
 - AAV, rabies virus, and CTB
 - Electrode construction for *in vivo* recording
 - Surgical procedures
 - Fiber recording
 - *In vivo* electrophysiological recording
 - Optogenetic identification of SuM^{CA2} or SuM^{DG} projecting neurons
 - Tetrode recording in SuM
 - Local field potential recording in hippocampal CA2, CA1, or DG
 - Behavioral task procedure and analysis
 - Three-chamber social novelty test
 - Direct interaction test
 - Novel object place recognition test
 - Fear conditioning
 - Optogenetic silencing
 - Sleep structure analysis
 - Histology
- **QUANTIFICATION AND STATISTICAL ANALYSIS**
 - Data analysis and statistics

SUPPLEMENTAL INFORMATION

Supplemental information can be found online at <https://doi.org/10.1016/j.neuron.2022.09.004>.

ACKNOWLEDGMENTS

The authors are grateful to Ms. Jia Lou for help in composing and layout editing of the figures. This work was supported by grants from the National Key R&D Program of China (2021YFA0805000), the National Natural Science Foundation of China (31925018, 32127801, 31921003, and 61890952), Chongqing Basic Research grants (cstc2019jcyjX0001), Guangxi Science and Technology Base and Talents Fund (GUIKE AD22035948) to X.C., and the National Key R&D Program of China (2018YFA0109600) to K.Z. X.C. is a member of the CAS Center for Excellence in Brain Science and Intelligence Technology. A.K. is a Hertie Senior Professor of Neuroscience.

AUTHOR CONTRIBUTIONS

Project design, H.Q., L.F., and X.C.; injection and histology, H.Q., T.J., J.L., Q.C., X.Y., H.D., and J.Y.; behavior experiments, H.Q., T.J., M.L., and Q.C.; EEG and EMG recordings, H.Q., T.J., M.L., and S.R.; electrophysiology, H.Q., W.J., T.J., M.L., and B.H.; fiber recordings, H.Q., T.J., and J.L.; data interpretation and analysis, H.Q., L.F., X.L., K.Z., R.W., S.L., C.Z., Y.W., Z.H., H.J., A.K., and X.C.; figure preparation, H.Q. and X.C.; manuscript writing, H.Q., A.K., and X.C. with the help of all co-authors. All authors read and commented on the manuscript.

DECLARATION OF INTERESTS

The authors declare no competing interests.

Received: January 26, 2022

Revised: July 29, 2022

Accepted: September 2, 2022

Published: October 21, 2022

REFERENCES

- Alexander, G.M., Farris, S., Pirone, J.R., Zheng, C., Colgin, L.L., and Dudek, S.M. (2016). Social and novel contexts modify hippocampal CA2 representations of space. *Nat. Commun.* 7, 10300. <https://doi.org/10.1038/ncomms10300>.
- Antunes, M., and Biala, G. (2012). The novel object recognition memory: neurobiology, test procedure, and its modifications. *Cogn. Process.* 13, 93–110. <https://doi.org/10.1007/s10339-011-0430-z>.
- Billwiller, F., Castillo, L., Elseedy, H., Ivanov, A.I., Scapula, J., Ghestem, A., Carponcy, J., Libourel, P.A., Bras, H., Abdelmeguid, N.E., et al. (2020). GABA-glutamate supramammillary neurons control theta and gamma oscillations in the dentate gyrus during paradoxical (REM) sleep. *Brain Struct. Funct.* 225, 2643–2668. <https://doi.org/10.1007/s00429-020-02146-y>.
- Blumberg, M.S., Lesku, J.A., Libourel, P.A., Schmidt, M.H., and Rattenborg, N.C. (2020). What is REM sleep? *Curr. Biol.* 30, R38–r49. <https://doi.org/10.1016/j.cub.2019.11.045>.
- Born, J., Rasch, B., and Gais, S. (2006). Sleep to remember. *Neuroscientist* 12, 410–424. <https://doi.org/10.1177/1073858406292647>.
- Boyce, R., Glasgow, S.D., Williams, S., and Adamantidis, A. (2016). Causal evidence for the role of REM sleep theta rhythm in contextual memory consolidation. *Science* 352, 812–816. <https://doi.org/10.1126/science.aad5252>.
- Broussard, G.J., Liang, Y., Fridman, M., Unger, E.K., Meng, G., Xiao, X., Ji, N., Petreanu, L., and Tian, L. (2018). *In vivo* measurement of afferent activity with axon-specific calcium imaging. *Nat. Neurosci.* 21, 1272–1280. <https://doi.org/10.1038/s41593-018-0211-4>.
- Buzsáki, G. (2015). Hippocampal sharp wave-ripple: a cognitive biomarker for episodic memory and planning. *Hippocampus* 25, 1073–1188. <https://doi.org/10.1002/hipo.22488>.
- Buzsáki, G. (1989). Two-stage model of memory trace formation: a role for “noisy” brain states. *Neuroscience* 31, 551–570. [https://doi.org/10.1016/0306-4522\(89\)90423-5](https://doi.org/10.1016/0306-4522(89)90423-5).
- Buzsáki, G. (2002). Theta oscillations in the hippocampus. *Neuron* 33, 325–340. [https://doi.org/10.1016/s0896-6273\(02\)00586-x](https://doi.org/10.1016/s0896-6273(02)00586-x).

- Chen, S., He, L., Huang, A.J.Y., Boehringer, R., Robert, V., Wintzer, M.E., Polygalov, D., Weitemier, A.Z., Tao, Y., Gu, M., et al. (2020). A hypothalamic novelty signal modulates hippocampal memory. *Nature* 586, 270–274. <https://doi.org/10.1038/s41586-020-2771-1>.
- Dana, H., Sun, Y., Mohar, B., Hulse, B.K., Kerlin, A.M., Hasseman, J.P., Tsegaye, G., Tsang, A., Wong, A., Patel, R., et al. (2019). High-performance calcium sensors for imaging activity in neuronal populations and microcompartments. *Nat. Methods* 16, 649–657. <https://doi.org/10.1038/s41592-019-0435-6>.
- Diekelmann, S., and Born, J. (2010). The memory function of sleep. *Nat. Rev. Neurosci.* 11, 114–126. <https://doi.org/10.1038/nrn2762>.
- Donegan, M.L., Stefanini, F., Meira, T., Gordon, J.A., Fusi, S., and Siegelbaum, S.A. (2020). Coding of social novelty in the hippocampal CA2 region and its disruption and rescue in a 22q11.2 microdeletion mouse model. *Nat. Neurosci.* 23, 1365–1375. <https://doi.org/10.1038/s41593-020-00720-5>.
- Ego-Stengel, V., and Wilson, M.A. (2010). Disruption of ripple-associated hippocampal activity during rest impairs spatial learning in the rat. *Hippocampus* 20, 1–10. <https://doi.org/10.1002/hipo.20707>.
- Farrell, J.S., Lovett-Barron, M., Klein, P.M., Sparks, F.T., Gschwind, T., Ortiz, A.L., Ahanonu, B., Bradbury, S., Terada, S., Oijala, M., et al. (2021). Supramammillary regulation of locomotion and hippocampal activity. *Science* 374, 1492–1496. <https://doi.org/10.1126/science.abh4272>.
- Fernandez-Lamo, I., Gomez-Dominguez, D., Sanchez-Aguilera, A., Oliva, A., Morales, A.V., Valero, M., Cid, E., Berenyi, A., and Menendez de la Prida, L. (2019). Proximodistal Organization of the CA2 Hippocampal Area. *Cell Rep.* 26, 1734–1746.e6. <https://doi.org/10.1016/j.celrep.2019.01.060>.
- Fernandez-Ruiz, A., Oliva, A., Fermino de Oliveira, E., Rocha-Almeida, F., Tingley, D., and Buzsaki, G. (2019). Long-duration hippocampal sharp wave ripples improve memory. *Science* 364, 1082–1086. <https://doi.org/10.1126/science.aax0758>.
- Girardeau, G., Benchenane, K., Wiener, S.I., Buzsaki, G., and Zugaro, M.B. (2009). Selective suppression of hippocampal ripples impairs spatial memory. *Nat. Neurosci.* 12, 1222–1223. <https://doi.org/10.1038/nn.2384>.
- Girardeau, G., and Lopes-dos-Santos, V. (2021). Brain neural patterns and the memory function of sleep. *Science* 374, 560–564. <https://doi.org/10.1126/science.abi8370>.
- Govorunova, E.G., Sineshchekov, O.A., Janz, R., Liu, X., and Spudich, J.L. (2015). Natural light-gated anion channels: a family of microbial rhodopsins for advanced optogenetics. *Science* 349, 647–650. <https://doi.org/10.1126/science.aaa7484>.
- Gunaydin, L., Grosenick, L., Finkelstein, J., Kauvar, I., Fenno, L., Adhikari, A., Lammel, S., Mirzabekov, J., Airan, R., Zalocusky, K., et al. (2014). Natural neural projection dynamics underlying social behavior. *Cell* 157, 1535–1551. <https://doi.org/10.1016/j.cell.2014.05.017>.
- Hazan, L., Zugaro, M., and Buzsaki, G. (2006). Klusters, NeuroScope, NDManager: a free software suite for neurophysiological data processing and visualization. *J. Neurosci. Meth.* 155, 207–216. <https://doi.org/10.1016/j.jneumeth.2006.01.017>.
- Hitti, F.L., and Siegelbaum, S.A. (2014). The hippocampal CA2 region is essential for social memory. *Nature* 508, 88–92. <https://doi.org/10.1038/nature13028>.
- Ishikawa, A., Kanayama, Y., Matsumura, H., Tsuchimochi, H., Ishida, Y., and Nakamura, S. (2006). Selective rapid eye movement sleep deprivation impairs the maintenance of long-term potentiation in the rat hippocampus. *Eur. J. Neurosci.* 24, 243–248. <https://doi.org/10.1111/j.1460-9568.2006.04874.x>.
- Ito, H.T., Moser, E.I., and Moser, M.B. (2018). Supramammillary nucleus modulates spike-time coordination in the prefrontal-thalamo-hippocampal circuit during navigation. *Neuron* 99, 576–587.e5. <https://doi.org/10.1016/j.neuron.2018.07.021>.
- Izawa, S., Chowdhury, S., Miyazaki, T., Mukai, Y., Ono, D., Inoue, R., Ohmura, Y., Mizoguchi, H., Kimura, K., Yoshioka, M., et al. (2019). REM sleep-active MCH neurons are involved in forgetting hippocampus-dependent memories. *Science* 365, 1308–1313. <https://doi.org/10.1126/science.aax9238>.
- Kogan, J.H., Frankland, P.W., and Silva, A.J. (2000). Long-term memory underlying hippocampus-dependent social recognition in mice. *Hippocampus* 10, 47–56. [https://doi.org/10.1002/\(sici\)1098-1063\(2000\)10:1<47::aid-hipo5>3.0.co;2-6](https://doi.org/10.1002/(sici)1098-1063(2000)10:1<47::aid-hipo5>3.0.co;2-6).
- Kumar, D., Koyanagi, I., Carrier-Ruiz, A., Vergara, P., Srinivasan, S., Sugaya, Y., Kasuya, M., Yu, T.S., Vogt, K.E., Muratani, M., et al. (2020). Sparse activity of hippocampal adult-born neurons during rem sleep is necessary for memory consolidation. *Neuron* 107, 552–565.e10. <https://doi.org/10.1016/j.neuron.2020.05.008>.
- Lai, W.S., Ramiro, L.L., Yu, H.A., and Johnston, R.E. (2005). Recognition of familiar individuals in golden hamsters: a new method and functional neuroanatomy. *J. Neurosci.* 25, 11239–11247. <https://doi.org/10.1523/jneurosci.2124-05.2005>.
- Lein, E.S., Callaway, E.M., Albright, T.D., and Gage, F.H. (2005). Redefining the boundaries of the hippocampal CA2 subfield in the mouse using gene expression and 3-dimensional reconstruction. *J. Comp. Neurol.* 485, 1–10. <https://doi.org/10.1002/cne.20426>.
- Li, Y., Bao, H., Luo, Y., Yoan, C., Sullivan, H.A., Quintanilla, L., Wickersham, I., Lazarus, M., Shih, Y.Y.I., and Song, J. (2020). Supramammillary nucleus synchronizes with dentate gyrus to regulate spatial memory retrieval through glutamate release. *Elife* 9, e53129. <https://doi.org/10.7554/elife.53129>.
- Liu, D., Li, W., Ma, C., Zheng, W., Yao, Y., Tso, C.F., Zhong, P., Chen, X., Song, J.H., Choi, W., et al. (2020). A common hub for sleep and motor control in the substantia nigra. *Science* 367, 440–445. <https://doi.org/10.1126/science.aaz0956>.
- Liu, K., Kim, J., Kim, D.W., Zhang, Y.S., Bao, H., Denaxa, M., Lim, S.A., Kim, E., Liu, C., Wickersham, I.R., et al. (2017). Lhx6-positive GABA-releasing neurons of the zona incerta promote sleep. *Nature* 548, 582–587. <https://doi.org/10.1038/nature23663>.
- Lu, J., Sherman, D., Devor, M., and Saper, C.B. (2006). A putative flip-flop switch for control of REM sleep. *Nature* 441, 589–594. <https://doi.org/10.1038/nature04767>.
- Maquet, P. (2001). The role of sleep in learning and memory. *Science* 294, 1048–1052. <https://doi.org/10.1126/science.1062856>.
- Maquet, P., Péters, J.M., Aerts, J., Delfiore, G., Degueldre, C., Luxen, A., and Franck, G. (1996). Functional neuroanatomy of human rapid-eye-movement sleep and dreaming. *Nature* 383, 163–166. <https://doi.org/10.1038/383163a0>.
- Marshall, L., and Born, J. (2007). The contribution of sleep to hippocampus-dependent memory consolidation. *Trends Cogn. Sci.* 11, 442–450. <https://doi.org/10.1016/j.tics.2007.09.001>.
- Meira, T., Leroy, F., Buss, E.W., Oliva, A., Park, J., and Siegelbaum, S.A. (2018). A hippocampal circuit linking dorsal CA2 to ventral CA1 critical for social memory dynamics. *Nat. Commun.* 9, 4163. <https://doi.org/10.1038/s41467-018-06501-w>.
- Moy, S.S., Nadler, J.J., Perez, A., Barbaro, R.P., Johns, J.M., Magnuson, T.R., Piven, J., and Crawley, J.N. (2004). Sociability and preference for social novelty in five inbred strains: an approach to assess autistic-like behavior in mice. *Genes Brain Behav* 3, 287–302. <https://doi.org/10.1111/j.1601-1848.2004.00076.x>.
- Okuyama, T., Kitamura, T., Roy, D.S., Itohara, S., and Tonegawa, S. (2016). Ventral CA1 neurons store social memory. *Science* 353, 1536–1541. <https://doi.org/10.1126/science.aaf7003>.
- Oliva, A., Fernandez-Ruiz, A., Leroy, F., and Siegelbaum, S.A. (2020). Hippocampal CA2 sharp-wave ripples reactivate and promote social memory. *Nature* 587, 264–269. <https://doi.org/10.1038/s41586-020-2758-y>.
- Pan, W.X., and McNaughton, N. (2004). The supramammillary area: its organization, functions and relationship to the hippocampus. *Prog. Neurobiol.* 74, 127–166. <https://doi.org/10.1016/j.pneurobio.2004.09.003>.
- Pedersen, N.P., Ferrari, L., Venner, A., Wang, J.L., Abbott, S.B.G., Vujovic, N., Arrigoni, E., Saper, C.B., and Fuller, P.M. (2017). Supramammillary glutamate neurons are a key node of the arousal system. *Nat. Commun.* 8, 1405. <https://doi.org/10.1038/s41467-017-01004-6>.

- Pfeiffer, B.E. (2020). The content of hippocampal "replay". *Hippocampus* 30, 6–18. <https://doi.org/10.1002/hipo.22824>.
- Phillips, M.L., Robinson, H.A., and Pozzo-Miller, L. (2019). Ventral hippocampal projections to the medial prefrontal cortex regulate social memory. *Elife* 8, e44182. <https://doi.org/10.7554/elife.44182>.
- Qin, H., Fu, L., Hu, B., Liao, X., Lu, J., He, W., Liang, S., Zhang, K., Li, R., Yao, J., et al. (2018). A visual-cue-dependent memory circuit for place navigation. *Neuron* 99, 47–55.e4. <https://doi.org/10.1016/j.neuron.2018.05.021>.
- Rasch, B., and Born, J. (2013). About sleep's role in memory. *Physiol. Rev.* 93, 681–766. <https://doi.org/10.1152/physrev.00032.2012>.
- Ren, S., Wang, Y., Yue, F., Cheng, X., Dang, R., Qiao, Q., Sun, X., Li, X., Jiang, Q., Yao, J., et al. (2018). The paraventricular thalamus is a critical thalamic area for wakefulness. *Science* 362, 429–434. <https://doi.org/10.1126/science.aat2512>.
- Renouard, L., Billwiller, F., Ogawa, K., Clement, O., Camargo, N., Abdelkarim, M., Gay, N., Scote-Blachon, C., Toure, R., Libourel, P.A., et al. (2015). The supramammillary nucleus and the claustrum activate the cortex during REM sleep. *Sci. Adv.* 1, e1400177. <https://doi.org/10.1126/sciadv.1400177>.
- Robert, V., Therreau, L., Chevalyere, V., Lepicard, E., Viollet, C., Cognet, J., Huang, A.J., Boehringer, R., Polygalov, D., McHugh, T.J., and Piskorowski, R.A. (2021). Local circuit allowing hypothalamic control of hippocampal area CA2 activity and consequences for CA1. *Elife* 10, e63352. <https://doi.org/10.7554/elife.63352>.
- Schmitzer-Torbert, N., and Redish, A.D. (2004). Neuronal activity in the rodent dorsal striatum in sequential navigation: separation of spatial and reward responses on the multiple T task. *J. Neurophysiol.* 91, 2259–2272. <https://doi.org/10.1152/jn.00687.2003>.
- Stark, E., Koos, T., and Buzsaki, G. (2012). Diode probes for spatiotemporal optical control of multiple neurons in freely moving animals. *J. Neurophysiol.* 108, 349–363. <https://doi.org/10.1152/jn.00153.2012>.
- Stickgold, R. (2005). Sleep-dependent memory consolidation. *Nature* 437, 1272–1278. <https://doi.org/10.1038/nature04286>.
- Thor, D.H., and Holloway, W.R. (1982). Social memory of the male laboratory rat. *J. Comp. Physiol. Psychol.* 96, 1000–1006. <https://doi.org/10.1037/0735-7036.96.6.1000>.
- Van Dort, C.J., Zachs, D.P., Kenny, J.D., Zheng, S., Goldblum, R.R., Gelwan, N.A., Ramos, D.M., Nolan, M.A., Wang, K., Weng, F.J., et al. (2015). Optogenetic activation of cholinergic neurons in the PPT or LDT induces REM sleep. *Proc. Natl. Acad. Sci. USA* 112, 584–589. <https://doi.org/10.1073/pnas.1423136112>.
- Vertes, R.P. (1992). PHA-L analysis of projections from the supramammillary nucleus in the rat. *J. Comp. Neurol.* 326, 595–622. <https://doi.org/10.1002/cne.903260408>.
- Walker, M.P., and Stickgold, R. (2006). Sleep, memory, and plasticity. *Annu. Rev. Psychol.* 57, 139–166. <https://doi.org/10.1146/annurev.psych.56.091103.070307>.
- Wu, X., Morishita, W., Beier, K.T., Heifets, B.D., and Malenka, R.C. (2021). 5-HT modulation of a medial septal circuit tunes social memory stability. *Nature* 599, 96–101. <https://doi.org/10.1038/s41586-021-03956-8>.
- Zingg, B., Chou, X.L., Zhang, Z.G., Mesik, L., Liang, F., Tao, H.W., and Zhang, L.I. (2017). AAV-mediated anterograde transsynaptic tagging: mapping corticocollicular input-defined neural pathways for defense behaviors. *Neuron* 93, 33–47. <https://doi.org/10.1016/j.neuron.2016.11.045>.

STAR★METHODS

KEY RESOURCES TABLE

REAGENT or RESOURCE	SOURCE	IDENTIFIER
Antibodies		
rabbit anti-PCP4	Sigma-Aldrich	Cat# HPA005792; RRID: AB_1855086
chicken anti-GFP	Abcam	Cat# ab13970; RRID: AB_300798
Alexa Fluor 488 donkey anti-chicken	Sigma-Aldrich	Cat# SAB4600031; RRID: AB_2721061
Alexa Fluor 568 donkey anti-rabbit	Sigma-Aldrich	Cat# A10042; RRID: AB_2534017
Bacterial and virus strains		
AAV2/9-EF1 α -EGFP	Taitool Bioscience Co., Ltd.	Cat# S0243-9
AAV2/9-Syn-axon-jGCaMP7b	Taitool Bioscience Co., Ltd.	Cat# S0602-9
AAV2/2Retro Plus-Syn-Cre	Taitool Bioscience Co., Ltd.	Cat# S0278-2RP
AAV2/9-EF1 α -DIO-hChr2-mCherry	Obio Biotechnology Co., Ltd.	Cat# AG20297
AAV2/9-Syn-DIO-hGtACR1-mCherry	Taitool Bioscience Co., Ltd.	Cat# S0693-9
AAV2/9-Syn-DIO-mCherry	Taitool Bioscience Co., Ltd.	Cat# S0240-9
AAV2/9-hSyn-FLEX-GCaMP6f	Taitool Bioscience Co., Ltd.	Cat# S0227-9
scAAV2/1-hSyn-Cre	Taitool Bioscience Co., Ltd.	Cat# S0292-1
AAV2/5-Ef1 α -DIO-EGFP-2A-VTA	BrainVTA Co., Ltd.	Cat# PT-0062
AAV2/5-Ef1 α -DIO-RVG	BrainVTA Co., Ltd.	Cat# PT-0023
RV-ENVA- Δ G-DsRed	BrainVTA Co., Ltd.	Cat# R01002
Chemicals, peptides, and recombinant proteins		
CTB488	Thermo fisher	Cat# C34775
CTB555	Thermo fisher	Cat# C34776
Experimental models: Organisms/strains		
Mouse: C57BL/6J	Beijing HFK Bioscience Co., Ltd.	JAX: 000664; RRID: IMSR_JAX:000664
Software and algorithms		
MATLAB_R2016b	Mathworks	https://www2.mathworks.cn/products/matlab.html ; RRID: SCR_001622
LabVIEW 2014	National Instrument	http://www.ni.com/en-us/shop/labview/select-edition.html ; RRID: SCR_014325
IBM SPSS Statistics 22	IBM	https://www.ibm.com/products/spss-statistics ; RRID: SCR_016479
NeuroScope	Hazan et al., 2006	http://neurosuite.sourceforge.net
MClust	Schmitzer-Torbert and Redish, 2004	https://github.com/adredish/MClust-Spike-Sorting-Toolbox
Recording software	Intan Technologies	https://intantech.com/downloads.html?tabSelect=Software&Pos=0
Other		
Multimode optical fiber: MFP_200/230/900-0.48	Doric lenses	http://doriclenses.com/life-sciences/mono-fiber-optic/854-mono-fiber-optic-patch-cords-glass-048-053-na.html
473 nm solid-state laser: MBL-III-473	Changchun New Industries	http://www.cnlaser.com/blue_laser473.htm
16 channel digital amplifier: C3334	Intan Technology	http://intantech.com/RHD2132_16channel_amp_board.html
RHD2000 USB interface board: C3100	Intan Technology	http://intantech.com/RHD2000_USB_interface_board.html
Laser diode controller: LDC205C	Thorlabs	https://www.thorlabs.com/thorproduct.cfm?partnumber=LDC205C

RESOURCE AVAILABILITY

Lead contact

Further information and requests for resources and reagents should be directed to and will be fulfilled by the lead contact, Dr. Xiaowei Chen (xiaowei_chen@tmmu.edu.cn).

Materials availability

This study did not generate new unique reagents.

Data and code availability

- Data reported in this paper will be shared by the lead contact upon request.
- This paper does not report original code.
- Any additional information required to reanalyze the data reported in this paper is available from the [lead contact](#) upon request.

EXPERIMENTAL MODEL AND SUBJECT DETAILS

3–5-month-old adult male C57BL/6CJ mice were used for recording and behavioral experiments. Mice were housed in groups of 4–5, except for those with optical fiber and tetrode implants which were housed individually. Mice were given free access to food and water and were housed under a 12:12 h light/dark cycle (lights on at 7:00 a.m.). All experimental procedures were conducted according to the protocols and guidelines of the Third Military Medical University Animal Care and Use Committee.

METHOD DETAILS

AAV, rabies virus, and CTB

The following AAV virus constructs were used in this study: AAV2/8-EF1 α -EGFP (titer: 1.49×10^{13} viral particles/mL), AAV2/9-Syn-axon-jGCaMP7b (titer: 2.17×10^{13} viral particles/mL), AAV2/2Retro Plus-Syn-Cre (titer: 1.92×10^{13} viral particles/mL), AAV2/9-EF1 α -DIO-hChR2-mCherry (titer: 3.67×10^{13} viral particles/mL), AAV2/9-Syn-DIO-hGtACR1-mCherry (titer: 1.43×10^{13} viral particles/mL), AAV2/9-Syn-DIO-mCherry (titer: 1.23×10^{13} viral particles/mL), AAV2/5-Ef1 α -DIO-EGFP-2A-VTA (titer: 2.00×10^{12} viral particles/mL), AAV2/5-Ef1 α -DIO-RVG (titer: 2.00×10^{12} viral particles/mL), AAV2/9-FLEX-GCaMP6f (titer: 1.00×10^{13} viral particles/mL), and scAAV2/1-Cre (titer: 5.00×10^{12} viral particles/mL). All AAV constructs were purchased from Taitool Bioscience Co., Ltd. (Shanghai, China), BrainVTA Co., Ltd. (Wuhan China) or Obio Biotechnology Co., Ltd. (Shanghai, China). For rabies virus, the RV-ENVA- Δ G-DsRed (titer: 2.00×10^8 viral particles/mL) was purchased from BrainVTA Co., Ltd. (Wuhan China). CTB488 (0.2%, c34775, Thermo fisher) and CTB555 (0.2%, c34776, Thermo fisher) were used to identify SuM neurons that projected to CA2 and DG.

Electrode construction for *in vivo* recording

Custom-made tetrode was composed of four 25 μ m insulated tungsten wires (California Fine Wire). Four tetrodes were assembled in a line array every 200 μ m. The tetrodes were mounted onto a microdrive to allow vertical movement. For hippocampal CA2, CA1, and DG local field potential recording, each tetrode was spaced 200 μ m vertically. For tetrode recording in SuM, the four tetrodes were aligned at the end without spacing in the vertical direction. The optrodes consisted of four tetrodes and a 200 μ m-diameter fiber (NA 0.37). The previously described tetrodes were fixed to the optical fiber with the tips being \sim 500 μ m longer than the fiber end. A laser diode was attached to the opposite end of the optical fiber and the laser intensity from the fiber was measured before connecting with super glue. Electrodes for EEG-EMG recording were attached for synchronous recordings.

Surgical procedures

For virus injection, 2–3-month-old mice were anesthetized with isoflurane in oxygen (induced at 3%, maintained at 1–2%) and placed into a stereotaxic frame with a heating pad (37.5–38°C) to keep them warm. A glass pipette with a tip diameter of 10–20 μ m was used to deliver the virus to a particular brain location. To express EGFP or jGCaMP7b in the SuM-DG and SuM-CA2 projections, AAV-EGFP (30–50 nL) or AAV-axon-jGCaMP7b (100–200 nL) was injected into SuM (AP: -2.8 mm, ML: 0.5 mm, DV: 5.0 mm from dura). To express ChR2, hGtACR1, or mCherry in the SuM-CA2 or SuM-DG projections, AAV2/2Retro-Cre was injected into CA2 (AP: -1.8 mm, ML: 2.45 mm, DV: 1.55 mm, 100–200 nL) or DG (AP: -1.8 mm, ML: 1.1 mm, DV: 1.85 mm, 100–200 nL), and AAV-DIO-ChR2-mCherry, AAV-DIO-hGtACR1-mCherry, or AAV-DIO-mCherry were injected into SuM (100–200 nL). To express GCaMP6f in DG or CA2 neurons that receiving inputs from SuM, AAV2/9-FLEX-GCaMP6f was injected into CA2 (AP: -1.8 mm, ML: 2.45 mm, DV: 1.55 mm, 100–200 nL) or DG (AP: -1.8 mm, ML: 1.1 mm, DV: 1.85 mm, 100–200 nL), and scAAV2/1-Cre was injected into SuM (100–200 nL). For optrode recording and histological tracing experiments, the viruses were injected unilaterally, and for behavioral experiments the viruses were injected bilaterally. The viruses were allowed to express at least one month prior to subsequent histological recording and behavioral experiments.

To implant fibers in axon terminals of the SuM-CA2 or SuM-DG projections, mice were placed in a stereotactic frame after anesthesia with 1–2% isoflurane in oxygen. An optical fiber (200 μm diameter, NA 0.53, Doric lenses, MFP_200/230/900–0.53) was glued into a mental cannula (ID. 0.51 mm, OD. 0.82 mm) after cutting the end face flat. The prepared fiber was inserted through a small cranial window above CA2 (AP: -1.8 mm, ML: 2.5 mm, DV: 1.5 mm) or DG (AP: -1.8 mm, ML: 1.1 mm, DV: 1.8 mm). The cannula was then secured to the skull using blue light-curing dental cement (Tetric EvoFlow, 595989WW). Common dental cement and super glue were used for further reinforcement and a thin layer of black acrylic paint was applied evenly to the outermost layer to avoid light pollution. After surgery, mice were individually housed with heating to allow for full recovery.

To implant EEG-EMG electrodes, three EEG stainless steel screws were inserted into the craniotomy holes. Two were placed above the frontal lobe (AP 1.5 mm, ML ± 1.5 mm) and one above the parietal lobe (AP -3.0 mm, ML 3.0 mm). Two EMG electrodes were inserted into the neck musculature and the incision was closed. A thin layer of blue light-curing dental cement was applied to fix the EEG screws and EMG wires. Additional dental cement and super glue were used to fix and strengthen the EEG-EMG connection with the skull.

For fiber ferrule implantation in optical silencing experiments, mice expressing GtACR1-mCherry or mCherry in bilateral SuM-CA2 or SuM-DG projections were used. Optical fiber ferrules (200 μm diameter, NA 0.37) were implanted with the tips placed above the bilateral SuM (AP -2.8 mm, ML ± 2.0 mm, at a 20° angle toward the midline, 4.6 mm depth). Mice were allowed to recover for at least 5 days prior to behavioral experiments. After behavioral experiments the locations of fiber tips were verified by post-hoc histology (Figures S7C and S7D).

To implant tetrodes in SuM, the previously described electrode was inserted above SuM (AP -2.8 mm, ML 0.5 mm) to a depth of 4.7 mm. After 5 days of recovery, the tetrode was gradually advanced to the target depth of ~ 5.0 mm.

To implant optrodes in SuM, mice expressing ChR2 in the SuM-DG or SuM-CA2 projection were used. The previously described optrode was inserted above SuM (AP -2.8 mm, ML 0.5 mm) to a depth of 4.7 mm. After 5 days of recovery, the optrode was gradually advanced to the target depth of ~ 5.0 mm.

To implant tetrodes in the hippocampal CA2, CA1, or DG, mice expressing GtACR1 in the SuM-DG or SuM-CA2 projection were used. The previously described electrode was inserted above CA2 (AP -1.8 mm, ML 2.5 mm) to a depth of 1.5 mm, CA1 (AP -1.8 mm, ML 1.2 mm) to a depth of 1.2 mm, or DG (AP -1.8 mm, ML 0.8 mm) to a depth of 1.8 mm. Fiber ferrules were implanted above SuM bilaterally to deliver inhibition light. After 5 days of recovery, the recordings were conducted.

Fiber recording

After mice implanted with fibers in CA2 or DG projections had recovered from surgery, fiber photometry-based Ca^{2+} recording was performed. Neuronal Ca^{2+} and EEG-EMG signals, along with behavioral video recordings, were simultaneously captured across sleep-wakefulness cycles. Data acquisition was conducted at frequencies of 2000 Hz for Ca^{2+} signals, 200 Hz for EEG-EMG signals, and 25 Hz for videos. All Ca^{2+} and EEG-EMG signals and behavioral videos were synchronized offline with event marks.

In vivo electrophysiological recording

All electrophysiological recordings began after mice were fully recovered from surgery and habituated to the recording apparatus. Signals were acquired at a sample rate of 20 kHz on a RHD2000 USB board (Intan Technology, C3100). Electrophysiological recordings and EEG-EMG recordings, along with behavioral video recordings, were simultaneously conducted. After recording, an electrical lesion was made by passing a current (100 μA , 10 s) through the tetrodes to verify the recording locations (Figures S4A, S4B, S6A, S8D, and S8E).

Optogenetic identification of SuM^{CA2} or SuM^{DG} projecting neurons

To identify SuM^{CA2} or SuM^{DG} projecting neurons, a series of optogenetic excitation light pulses of 15 mW intensity, 10 ms duration, and 1 s interval were given to circuit-specific ChR2-expression mice. Units produced by light delivery having a short spike latency (<7 ms for all the units in our data) and a high response reliability ($>90\%$) were identified as ChR2-positive neurons (Figures S4C–S4E).

Tetrode recording in SuM

Custom-made tetrodes described above were used for recordings. Tetrode recording in SuM was conducted across sleep-wakefulness cycles in the initial 8 h of day 1 light phase. Between 7:00 a.m. to 8:00 a.m. on day 2, mice were placed into a chamber and allowed to freely explore with a novel mouse for 20 min. Then mice were immediately placed back to home cage after social exploration. Then tetrode recording in SuM along with EEG-EMG and behavioral video recordings were conducted again in the following 8 h (Figure S6B).

Local field potential recording in hippocampal CA2, CA1, or DG

The local field potential recordings in CA2, CA1, or DG were monitored to identify REM episodes. Blue light was continually delivered to SuM during REM sleep for 4 s after REM episodes were detected. For theta rhythm measurements from CA2 or CA1, the recording sites were placed at the stratum lacunosum moleculare layer (SLM) but not at the pyramidal cell layer, as the amplitude of theta activity is largest in the SLM layer according to previous studies (Buzsáki, 2002; Boyce et al., 2016; Fernandez-Lamo et al., 2019).

Behavioral task procedure and analysis

All mice underwent, at most, two behavioral tasks. Only one task for a particular memory type was used, and the contextual fear conditioning task was always used as the second task. Mice were handled for 5 min each day for 3 consecutive days prior to behavioral habituation.

Three-chamber social novelty test

The three-chamber social novelty test was used as a social memory test (Hitti and Siegelbaum, 2014; Phillips et al., 2019). A square open-topped box (75 × 50 × 40 cm) was divided into 3 equal-sized chambers by transparent plastic sheets. A 12 cm diameter, organic glass cylinder with air holes in the wall was used to hold the stimulus mouse. The task involved three phases: habituation, training, and testing. The task was carried out across 3 consecutive days between 7:00 a.m. to 8:00 a.m. On day 1 (habituation), the subject mouse was allowed to freely explore the arena containing empty cylinders in the lateral two chambers for 10 min. On day 2 (training), a stimulus mouse was put into the left or right cylinder (systematically alternated), the other cylinder left empty, and the subject mouse was placed into the arena and allowed to freely explore for 20 min. The subject mouse was returned to the home cage immediately and the EEG-EMG recording was monitored to manually identify REM episodes across the following 8 h (for memory consolidation happens in the initial several hours after memory encoding (Kumar et al., 2020)). For sleep structure analysis, the real-time sleep-wakefulness state was defined according to the criteria described below. In GtACR1 REM and mCherry REM groups, blue light was continually delivered to SuM by fiber ferrules from the time detecting REM sleep and until the end of REM sleep. In GtACR1 NREM/QW group mice, blue light was delivered during NREM sleep or QW periods for an equivalent cumulative amount of time as the GtACR1 REM or mCherry REM groups (the average total time for light delivery during NREM sleep was 1477 ± 63 s, and the average total time for QW was 690 ± 57 s). In GtACR1 NREM mice, blue light was delivered during a large fraction of NREM sleep periods (71 ± 3% of the total cumulative NREM sleep time). On day 3 (testing), the familiar mouse was placed randomly in either the left or right chamber while a novel mouse was placed in the other, after which the subject mouse was introduced and again allowed to explore freely for 20 min. A custom-written MATLAB program was used to automatically track the positions of the subject mouse. Time spent investigating the stimulus mouse was recorded based on the mouse trajectory and a social preference index was calculated using the equation:

$$\text{Social preference index} = \frac{((\text{time for novel mouse}) - (\text{time for familiar mouse}))}{((\text{time for novel mouse}) + (\text{time for familiar mouse}))}$$

Correlation analysis between social memory performance and total REM sleep time indicated a positive correlation (Figure S9G). Mice from control groups which were not affected by optogenetic manipulation were used for this analysis (49 mice).

Direct interaction test

This test was conducted to observe social interactions in detail, with a high magnification view to observe the specific social interactions (Hitti and Siegelbaum, 2014). The task was conducted from 7:00 a.m. to 8:00 a.m. across 3 consecutive days. On day 1 (habituation), the subject mouse was allowed to freely explore the clean cage for 5 min. On day 2 (training), a novel mouse was introduced to the cage, and the subject mouse was allowed to socialize with the stimulus mouse for 5 min. After training, the subject mouse was returned to the home cage. EEG-EMG recording and optogenetic silencing manipulation were conducted as described above during the following 8 h. On day 3 (testing), the subject mouse was again placed in the cage individually with either the previously introduced stimulus mouse or a novel mouse for a 5 min social interaction period. Mouse social interaction behaviors (anogenital and nose-to-nose sniffing, following, and allogrooming) were manually reviewed by experiment-blinded analysts through the recorded videos, and the time of interaction for each mouse was documented. The interaction index was calculated from interaction time in training and testing phases as:

$$\text{Social interaction index} = \frac{((\text{time for testing mouse}) - (\text{time for training mouse}))}{((\text{time for testing mouse}) + (\text{time for training mouse}))}$$

Novel object place recognition test

The novel object place recognition task (Boyce et al., 2016) was conducted in a square open field (50 × 50 × 40 cm) with distinct patterns attached to the walls. The task again involved three phases: habituation, training, and testing. The task was carried out across 3 consecutive days from 7:00 a.m. to 8:00 a.m. Mice were allowed to explore freely in the open field for 10 min on day 1 (habituation). On day 2 (training), two identical objects (A and B) were fixed randomly to two quadrants of the arena, and mice were allowed to explore for 20 min. Mice were then immediately returned to the home cage and the EEG-EMG recording was monitored to manually identify REM episodes during the following 8 h. Optogenetic silencing manipulation was conducted as described above. On the third day (testing), the object B was repositioned to another quadrant, while object A was left in the same position relative to the training day, and subject mice were introduced into the arena for a 20-min free exploration period (the object and space quadrants were systematically alternated). Behavioral videos for all mice were recorded by an infrared camera at 25 Hz with a spatial resolution of 1920 × 1080 (Cannon, XA-25). Time spent investigating each object (with nose sniffing at object) during the training and testing

phases were manually reviewed by experiment-blinded analysts through the recorded videos to assess object preference. The object B discrimination index was calculated using the following equation:

$$\text{Object B discrimination index} = ((\text{time for Object B}) - (\text{time for Object A})) / ((\text{time for Object B}) + (\text{time for Object A}))$$

Correlation analysis between spatial memory performance and total REM sleep time indicated a positive correlation (Figure S9H). Mice from control groups which were not affected by optogenetic manipulation were used for this analysis (33 mice).

Fear conditioning

The fear conditioning task was used as the final behavioral task for all mice to test memory evoked by context and cue induced responses following a standard protocol (Boyce et al., 2016) (see protocol diagram in Figure S12A). The task was conducted from 7:00–9:00 a.m. across two consecutive days. During the training session, the unconditioned stimulus (US, electrical shock, 2 s, 0.6 mA intensity) was applied immediately following the conditioned stimulus (CS, pure tone at 8964 Hz, 20 s, 70 dB SPL) after a baseline recording of 260 s. This pairing was repeated three times, with an interval of 180 s. Mice were immediately returned to the home cage for EEG-EMG recording and optogenetic silencing manipulation, conducted as described above, during the following 8 h. 24 h after training, mice were introduced back into the training box for a 10-min recording. A cued fear memory recall test was carried out 1 h after the contextual memory test in a novel chamber which was different from the training box in shape, size, landmarks, and material (Figure S12A right). 5 CS stimuli (pure tone at 8964 Hz, 20 s, 70 dB SPL, 180 s interval) were applied after a baseline recording of 260 s. All task scenes were recorded by infrared camera for offline freezing analysis. A self-written MATLAB program was used to track the body movement intensity. Freezing level was calculated based on body movement at a time bin of 20 s (Qin et al., 2018). Freezing data was further binned for statistical analysis (3 min in the training phase and 2 min in the contextual testing phase).

Optogenetic silencing

For optogenetic silencing experiments, blue (473 nm wavelength) light was delivered to the bilateral SuM area. The light intensity was adjusted to ~3 mW at the tip of each fiber ferrule. Light delivery was controlled using a self-designed program on the LabVIEW platform.

We did not apply optogenetic inhibition throughout the entire 8-h interval. We applied optogenetic inhibition only during REM or NREM sleep episodes. The average length of REM sleep episodes was 69 ± 3 s, and the average length NREM sleep was 90 ± 3 s in our datasets ($n = 36$ mice). Thus, the average light application time for each episode was shorter than 1.5 min. In addition, a similar inhibition protocol has been applied in previous publications (4-h (Boyce et al., 2016); 6-h (Kumar et al., 2020); 12-h (Izawa et al., 2019)).

Sleep structure analysis

All recorded EEG-EMG signals were filtered by a band-pass filter (EEG, 0.5–30 Hz; EMG, 10–70 Hz). The sleep-wakefulness state was automatically analyzed based on the spectral characteristics of EEG and integral amplitude of EMG using sleep analysis software (SleepSign for Animal, Kissei Comtec). States were analyzed by continuous non-overlapping epochs of 4 s. Wakefulness was defined by high EMG activity and low amplitude EEG activity. NREM sleep was defined by high amplitude and low frequency EEG activity (delta band, 0.5–4 Hz), as well as low amplitude EMG activity. REM sleep was defined by low-amplitude and high frequency EEG activity (theta band, 4–10 Hz), and no tonic EMG activity. The automatic analysis results were manually checked and corrected. Cumulative and episodic durations of wakefulness, NREM sleep, and REM sleep were summarized using a self-designed MATLAB program.

Histology

All mice after recording or behavioral tests were perfused with 4% paraformaldehyde (PFA) in PBS. The brains were dehydrated with 15% sucrose in PBS for 24 h and sectioned into 50 μm slices. After staining with DAPI, brain slices were mounted onto glass slides and imaged with a confocal (Zeiss, LSM 700) or wide field (Olympus, BX51) microscope. For immunohistochemistry, mice injected with AAV2/8-EF1 α -EGFP in SuM (expression for one month) or CTB in CA2 and DG (expression for 10 days) were perfused and sectioned as described above. The following primary antibodies were used: rabbit anti-PCP4 (1:500; Sigma, HPA005792), and chicken anti-GFP (1:200; Abcam, ab13970). For cell counting of CTB-labeled samples, we collected brain slices from AP -2.5 mm to AP -3.2 mm two weeks after CTB injection into DG and CA2. Slices were 50 μm in thickness. The numbers of red, green, or double labeled cells in SuM were counted manually by experimenters (Figures S3D–S3F). The accurate AP position was confirmed by DAPI staining and the summarized data is shown in Figures S3D–S3F. For estimating the fraction of GCaMP6f expressing neurons that were CA2 pyramidal neurons (Figure 8B), we combined the immunostaining image results stained by PCP4 and GCaMP6f. The fraction of CA2 pyramidal neurons was $88.0 \pm 2.1\%$ ($n = 5$ mice).

QUANTIFICATION AND STATISTICAL ANALYSIS

Data analysis and statistics

Fiber recording data were analyzed using a procedure similar to previous work (Qin et al., 2018). Briefly, all of the Ca²⁺ signals were low-pass filtered by Savitzky-Golay FIR smoothing filter with 50 side points and a third order polynomial. Then Ca²⁺ signals were

converted as $\Delta f/f = (f - f_{\text{baseline}})/f_{\text{baseline}}$, where the f_{baseline} is the baseline fluorescence taken during the current recording period. To quantify the Ca^{2+} signals during sleep-wakefulness cycles, the arousal state was identified by synchronous EEG-EMG recording, and the area under Ca^{2+} signals was used for statistical analysis.

The raw extracellular electrophysiological data were preprocessed as described previously (Qin et al., 2018) to extract the spikes. All of the events that exceeded an amplitude threshold within four standard deviations above the background were saved for subsequent spike sorting analysis. All detected events for each tetrode were sorted in the toolbox MClust based on the features of waveforms (Schmitzer-Torbert and Redish, 2004). For single unit activity analysis, cell classification was performed according to firing patterns. We calculated the firing rates of each cell in a sliding time bin of 2 s (0.1 s interval).

A self-designed MATLAB program was used to analyze the spectral profiles of local field potential (LFP) and EEG activities (Ren et al., 2018). The raw LFP and EEG data were calculated by fast Fourier transformation with a frequency resolution of 0.15 Hz. The particular frequency bands were binned in delta (1–4 Hz), theta (6–12 Hz), alpha (12–15 Hz) and beta (15–30 Hz) (Billwiller et al., 2020; Boyce et al., 2016). The mean power densities of LFP in the 4 s before, during, and after optogenetic silencing were compared (Figures 5D, 6D, S8C, and S8H).

Statistical tests were performed in MATLAB and SPSS software (Table S1). Data were first tested for normality and equal variance between groups. When both were achieved, parametric tests were used. When normality or equal variance between groups failed, non-parametric tests were used. For parametric tests, paired and unpaired t tests, RMs 1-way ANOVA with LSD post-hoc comparison, 1-way ANOVA with LSD post-hoc comparison and RMs two-way ANOVA with Sidak's post-hoc comparison were used. For non-parametric tests, Wilcoxon signed-rank test, Wilcoxon rank-sum test, Kruskal-Wallis test with Tukey post-hoc comparison, and Friedman's ANOVA test were used. All tests were two-tailed. All summary data are from individual mice, and represented as mean \pm SEM